POLITECNICO
MILANO 1863

SCUOLA DI INGEGNERIA INDUSTRIALE
E DELL'INFORMAZIONE

Analysis of degradation of lithium-ion batteries coming from real automotive application

Tesi di Laurea Magistrale in
Energy Engineering - Ingegneria Energetica

Gian Marco Trippetta, 945715

Advisor:
Prof. Claudio Rabissi

Co-advisors:
Ing. Gabriele Sordi

Academic year:
2021-2022

Abstract: With the ever-growing public and now commercial sentiment supporting the widespread adoption of low and zero-emission vehicles, it is unsurprising that Li-ion batteries, which currently assume the bulk of the cost of electrified vehicles (≈ 40% [56, 63]), have become prolific not only in the primary research literature but have also entered the general public consciousness [40]. This technology has become one of the most commonly used power sources in the new generation vehicles due to its characteristics of high energy density, high power density, low self-discharge rate, etc. [19]. However, battery life can barely satisfy the demand of users, restricting the further development of electric vehicles. For this reason battery aging mechanisms and the impact of battery degradation should be considered as major factors in the optimization of the battery design and management [24]. However, the detection and understanding of the aforementioned aging phenomena is a challenging task due to the inter-dependency of the various degradation mechanisms that manifest themselves by capacity and power fade [30].
Therefore, the aim of this work is to gain knowledge on long term battery degradation modes, by analysing multiple samples aged in real automotive applications. Adding on top of that a method for detecting degradation phenomena through physical parameters, calibrated with an optimization algorithm from a set of easily acquirable experimental measurements. Which will then formulate a generalized protocol able to give an esteem of the State of Health of heterogeneous battery samples. Finally, a deepening on the diagnostics of parallels of cells was performed as a first step towards the understanding of module testing methods.

Key-words: lithium-ion batteries, automotive degradation, electric vehicles, experimental testing, physical model

1. Introduction

Two of the main energy challenges the world is facing today are shifting electricity production from fossil fuels to sustainable energy sources, and moving ground transportation towards electrical propulsion with the use of electric vehicles (EVs) instead of cars powered by internal combustion engines (ICEs) [21]. To achieve both of these tasks, a suitable technology for energy storage is required. Yet, while in recent years we have seen very impressive progresses in the development of technology for harvesting sustainable energy, the development of storage devices is still lagging behind. Therefore, the development of batteries that can store sustainable

energy with long term stability, very prolonged cycle life and meeting environmental constraints is an important challenge for modern electrochemistry [21]. Li-ion batteries have an unmatchable combination of high energy and power density, making it the technology of choice for portable electronics, power tools, and hybrid/full electric vehicles [19]. The high energy efficiency of Li-ion batteries may also allow their use in various electric grid applications, including improving the quality of energy harvested from renewable sources, thus contributing to their more widespread use and building an energy-sustainable economy [19]. Therefore Li-ion batteries are of intense interest from both industry and government funding agencies, and research in this field has abounded in the recent years [44].

Within this framework, two main lines of research are currently into prominence, namely, the development of new materials for Li-ion batteries [21] and the comprehension of physical and chemical mechanisms interplay behind cells degradation [9]. The latter will be the focus of this work. Therefore, experimental evidence of degradation will be presented, with support of degradation modes widely reported in literature, by means of tests conducted on multiple samples aged in real automotive applications. On top of that, a diagnostic protocol, which allows for the identification and quantification of the extent of each degradation mode in Li-ion cells, is implemented.
The structure of the thesis is the following:

Chapter 1: description of the state of the art of lithium ion batteries technology with focus on lithium iron phosphate batteries (LFP) and its degradation modes.

Chapter 2: the testing station alongside the experimental techniques involved in this work are presented and characterized. Moreover, the physical model and the calibration algorithm are introduced.

Chapter 3: results of experimental tests on Beginning of Life (BoL) cells are reported and interpreted in order to establish the most significant measures to formulate a protocol for the characterization of the cells. Thus, the physical model is used alongside the calibration algorithm to quantify pristine cells parameters.

Chapter 4: End of Life (EoL) battery samples are tested and compared with BoL results, allowing for the analysis of residual performances and the interpretation of the occurred degradation mechanisms. Moreover, an optimization algorithm is introduced for the quantification of the main degradation parameters.

Chapter 5: deepening on the behaviour of cells in parallel configuration in preparation for future studies on non-invasive diagnostic methods for battery modules.

2. State of Art

Lithium-ion batteries (LIB) are an electrochemical device that can store electric energy as chemical energy and allow the conversion from one another exploiting the reduction – oxidation reactions of lithium ions. Whilst they became a reality in the 1970s with the first rechargeable prototypes [66], Li-ion batteries did not receive widespread commercialization until graphite was introduced as anode material and lithiated transition metal oxide was introduced as cathode [21].

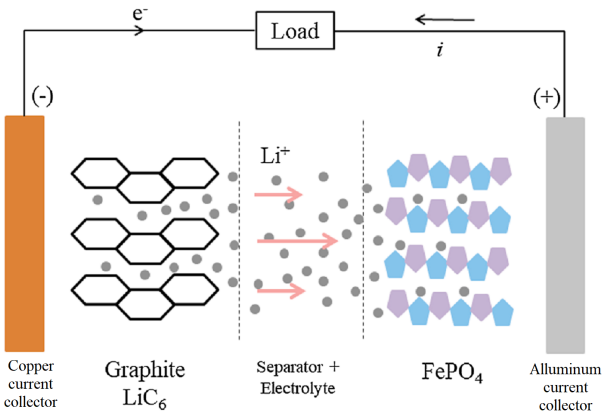

Figure 1: *Schematic of a LiFePO4 electrochemical cell [10].*

Figure 3 reports the structure of a LIB, a system made of two different electrodes, with many different materials combinations already thoroughly studied in literature [19, 21, 44, 69], interacting by means of a non-aqueous electrolyte and a separator that allow transport of Li-ions between them but avoid flow of electrons which would cause short circuits [6, 67]. Meanwhile the two current collectors, in aluminum (positive) and copper (negative) respectively, gather the electrons produced by the electrochemical reactions in the electrodes and allow for an external flow of electrons in a circuit connected to a load/charger.

2.1. Lithium iron phosphate battery

For the purpose of this work the main focus will be the lithium iron phosphate chemistry (LFP) being the type of sample analyzed in the experimental campaign. Therefore, $LiFePO_4$ will be presented as the constituent of the cathode while graphite (LiC_6) of the anode. The reactions that characterize the two electrodes during operation are the following:

$$Positive\,electrode:\ Li_{(y\text{-}z)}FePO4 + zLi^+ + ze^- \longrightarrow Li_yFePO4 \tag{1}$$

$$Negative\,electrode:\ xLiC_6 \longrightarrow Li_{x-z}C_6 + zLi^+ + ze^- \tag{2}$$

During discharge lithium ions (Li^+) and electrons (e^-) are released from the graphite (LiC_6) electrode. Li^+ moves within the electrolyte through the separator while e^- move towards the positive electrode through the external circuit. There they recombine allowing for the the lithiation of $FePO_4$.

$LiFePO_4$ manages to be amongst the group of commercial cathode chemistries, but still has a critical drawback. Its theoretical energy density is currently considered by most of the scientific community too limited (~ 170 mAh/g capacity respect ~ 285 mAh/g of a $LiMnO_2$ cathode [44]) for its desired applications. Furthermore the performances of the first $LiFePO_4$ cathodes were restricted by the poor electric conductivity (10^{-9} $S \cdot cm^{-1}$) of the active material. Recently, several innovations made it possible to enhance the conductivity of the cathodes significantly by fabricating cathodes with very small and carbon coated particles. Doping the bulk material with transition metal atoms (e.g. Mg, Ti, Nb, Zr, Al, W) led to a further improvement of cathodes performance [50]. Since LFP first appeared in 1997 [46], its chemical features have been thoroughly analyzed in literature. It owns an ordered olivine structure with a three dimensional framework consisting of distorted FeO_6 octahedra and PO_4 tetrahedra. Lithium ions are located and undergo transfer in one dimensional channels, and diffusion occurs along the crystallographic axis b in the materials with the olivine structure as shown in *Fig. 2* [45, 46].

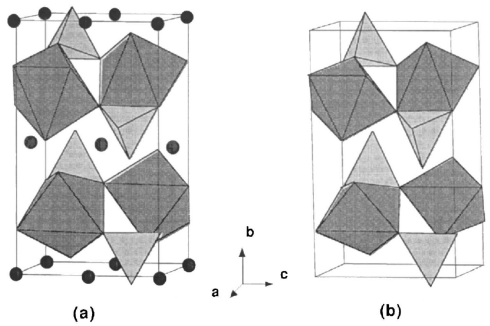

Figure 2: *Crystal structures of (a) $LiFePO_4$ and (b) $FePO_4$ [50].*

$LiFePO_4$ and $FePO_4$ almost possess the same structure (*see Fig. 2*). The small distinction between the two compounds results in only slight volume change and hence, no crystal structure damaging during charge and discharge process occurs. Differently from other cathode materials, the unique olivine structure of $LiFePO_4$ can assure an excellent stability and therefore a much longer lifetime [65]. In *Fig. 3a* the theoretical insertion and extraction process of a spherical particle is schematically depicted. During lithium insertion into a cathode particle (discharge) the particle's surface region becomes lithiated and two distinct phase regions (a lithiated phase and a delithiated phase region) emerge, within the originally homogeneous material, with a phase barrier between the two. Thereafter, one phase is transformed into its counterpart as Li insertion proceeds and the barrier propagates from the surface towards the center. Meanwhile the lithium concentration within each phase region remains constant. This two-phase transition continues until the particle is completely transformed. Analogously, during lithium de-insertion the particle's surface region becomes delithiated first while the phase barrier propagates towards the center until the particle is completely delithiated. The phase separation in the two-phase state is stable over time and hence, the phase barrier does not vanish through diffusion processes

during longer rest periods [51]. As already demonstrated by multiple literature sources [13, 14, 46, 50, 58] this two-phase transition can explain the phenomenon of super flat voltage plateau which is related to the constant Li concentration of the particles surface. In Li_xFePO_4 this effect happens between two molar fractions (x) in the possible range $0 \leq x \leq 1$, with different values reported in literature [22, 58]. For very low ($x \to 0$) and very high Li contents ($x \to 1$) instead the Li insertion/extraction homogeneously proceeds as a solid state reaction (*see Fig. 3b*) [51].

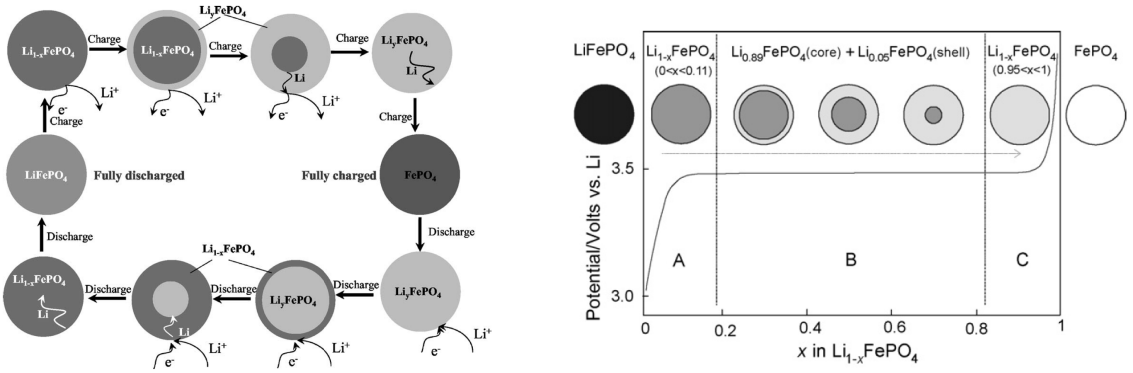

(a) *Schematic of the model that describes the juxtaposition of phases in the $LiFePO_4$ electrode; x and y have values close to zero. Both charge and discharge processes are described [59].*

(b) *Schematic presentation of occurrence of various phases during galvanostatic charge (discharge) of $LiFePO_4$ [22].*

Figure 3: *LFP electro-chemical characterization.*

Concerning the lithiated graphite anode (LiC_6) many literature works [5, 26, 71] present clearly and in detail the intercalation process of lithium in the aforementioned electrode. It occurs across four different stages via first-order phase transition reactions between them as in *Figure 4*.
spiegare altro su grafite

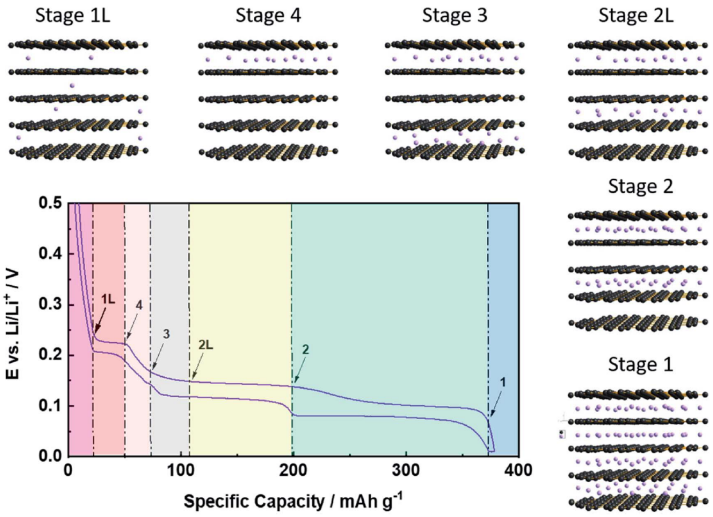

Figure 4: *Illustration of the staging mechanism for the electrochemical de-/intercalation of lithium cations (purple spheres) into graphite [5].*

Mixtures of alkyl carbonates including ethylene carbonate (EC), dimethyl (DMC), diethyl (DEC), and ethylmethyl (EMC) carbonates, and $LiPF_6$ (dithium hexafluorophosphate) salt as are currently used as LIB electrolyte solutions. The former is a mandatory component for sufficient negative electrode passivation while the latter, is chosen as a comprime respect the many disadvantages of the other options like: $LiAsF_6$ (poisonous), $LiClO_4$ (explosive), $LiBF_4$ (side reactions on negative side) as well as others [6]. Likewise, the electrolyte employed in the cell has been found to be $LiPF_6$ [10, 38, 48, 61] dissolved in a mixture of organic compounds of unknown proportions. Chiew *et al.* [10] work with a mixture of 2:1 EC/DMC, Prada *et al.* [48] report EMC and

DMC as the main components (ratio 1:1 (w:w)) of the mixture while Li *et al.* [38, 61] indicate PC(propylene carbonate)/EC/DMC (10:27:63 by volume) as solvent. These different options have been evaluated and compared in this work for a proper selection of parameters for the Li-ion battery model definition (*see Tab.* **??**).

2.2. Degradation modes

Degradation in Li-ion cells is caused by a large number of physical and chemical mechanisms, which affect the different components of the cells: the electrodes, the electrolyte, the separator and the current collectors. *Fig. 5* illustrates some of the most commonly reported degradation mechanisms in Li-ion cells. The different causes, rates and inter-dependencies of these degradation mechanisms make them extremely challenging to model, which is why most physics-based models focus only on the most dominant mechanisms, such as the formation and growth of the solid electrolyte interphase (SEI) [9, 62]. The latter consist in the formation of a passivation protective layer on the surface of the graphite electrode by reaction between the liquid electrolyte and the electron-conductive surface of the negative electrode (NE) [24]. This results in *ca.* 10% reduction in capacity on the first cycle of the cell, but then serves to stop further reaction of the electrolyte at the NE. However, as will be explained in the next paragraph, the thickness of the SEI layer increases as the cell ages causing additional performance limitations due to increasing resistive effects [20] In this work, the dual-tank model was selected, being one of the most common approach when it comes to the description and quantification of the main LIB degradation mechanisms that occur upon aging. Within this representation of the system, the active material of each electrode is like a tank, and the lithium ions are like a fluid exchanged between the two tanks. Therefore, the loss of lithium inventory (LLI) groups mechanisms resulting in a reduction of the amount of cyclable lithium available for transport between electrodes and hence a loss of the total fluid in the tanks. Meanwhile, the loss of active material (LAM), occurring in both positive (LAMp) and negative (LAMn) electrodes, groups mechanisms which lead to a reduction of the material available for charge and discharge and hence a change of the tanks capacities [20, 24]. This approach allows for the description of the degradation state with the use of only three parameters which will be useful for the physical model (*see Section 3.4*).

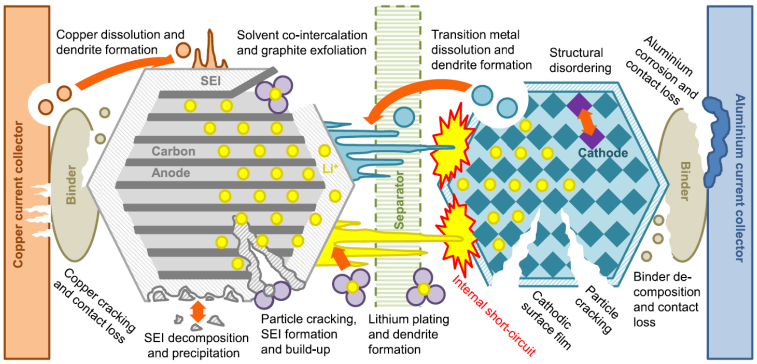

Figure 5: *Degradation mechanisms in Li-ion cells [9].*

For the sake of this work, a short deepening on the degradation characteristics of LFP cells will be carried out following the works of Li *et al.* [33–37] where degradation modes are presented with the support of extensive experimental measurements. In these papers a subdivision in two groups is made between storage and cycling induced ageing as it is represented in *Figure 6a* and *Figure 6b* respectively. Storage is mainly characterized by SEI thickening which is enhanced at conditions of State of Charge (SoC) > 50. Since the solvent is able to reach the SEI inner interface undisturbed, there it can be reduced by an electron (e^-) escaped (also known as electron tunneling) from the negative electrode (*see Figure 6a*). Alongside the release of the electron, oxidation reaction of lithium stored inside the graphite results in a free Li^+ ion that can eventually be immobilization in the SEI layers and hence cause irreversible capacity losses (LLI). Cycling-related ageing is instead characterized by the same phenomena of storage plus an additional effect related to volumetric shrinkage/expansion during operation (*see Section 2.1*). These volumetric changes result in mechanical stress, creating cracks in the SEI layers and therefore inducing the formation of uncovered graphite surface (A^{fr} *in Fig. 6b*) where the solvent is directly brought in contact with pristine graphite and is immediately reduced, leading to production of new SEI. An additional degradation mode which happens in both cases but only at specific conditions is the formation of metallic iron clusters at the anode (*see Fig. 6c*). This complex mechanism starts with cathode dissolution at high temperatures ($> 60°C$) combined with proton exchange between its products and water traces in the electrolyte. Fe^{2+} ions are produced and then subsequently transported to the anode where they are reduced at

the graphite surface. This causes multiple effects as Li^+ ion are released from cathode during iron dissolution and from the anode during its reduction, all contributing on LLI. Furthermore,the iron clusters deposited on the graphite surface can facilitate the SEI development by improving electron transport and in the meanwhile they can obstruct the covered graphite layers which become inactive causing additional loss of active material in the negative electrode. Even though not mentioned in the previously analyzed research works by Li *et al.*, many additional degradation mechanisms occur in LIB (*see Fig. 5*). One of them is lithium plating, a side reaction where metallic Li forms on the surface of the NE instead of intercalating into it. This can be caused by the NE surface becoming fully lithiated, in which the Li has nowhere else to go (thermodynamic plating), or by fast charging, where the high electrolyte potential increases the rate of the side reaction relative to the main intercalation reaction (kinetic plating). Even at moderate charge rates, below freezing temperatures slow down the main intercalation reaction enough to cause plating [4, 20].

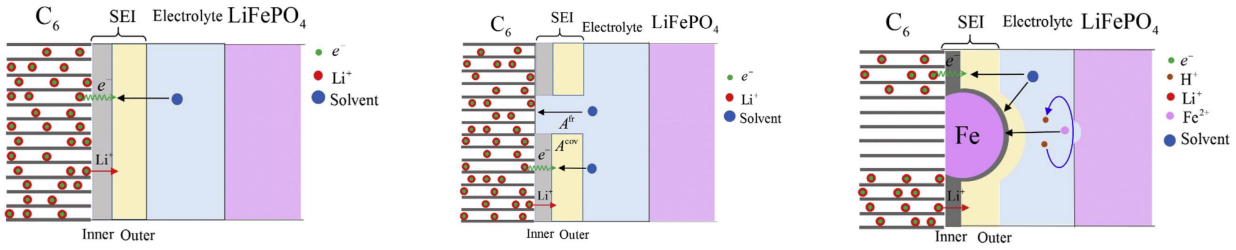

Figure 6: *Schematic representation of SEI formation on the graphite electrode inside a LFP battery under storage (a) and cycling (b) conditions. (c) The influence of elevated temperatures on aging processes inside LFP batteries [36].*

2.3. Aim of the thesis

This thesis work was carried out at the MRT Fuel Cell & Battery Laboratory of Politecnico di Milano starting in March 2022. Its main focus is the adaptation of already pre-existing diagnostic methods, developed in the past years within multiple thesis works [12, 29, 55], to a completely new battery chemistry (LFP) and with samples that have undergone real automotive operation for multiple years. Part of the work was developed with the support of the CIRC-eV laboratory within the Mechanical Engineering Department as part of a bigger collaboration focused on the study of "Circular Factory for the Electrified Vehicles of the Future". Moreover, the goals of this dissertation will be:

- Gain knowledge on the state of art of $LiFePO_4$ chemistry, its degradation modes and the most appropriate diagnostic techniques;
- Upgrade of the experimental testing station both for an increased number of tested cells as well as for higher voltage and power thresholds;
- Analysis of the aging state of cells coming from real use to understand which degradation mechanisms and with what intensity, through:
    - Experimental characterization of the performance of BoL devices;
    - Formulation of a diagnostic protocol capable of mapping the cell's conditions with a limited number of measurements;
    - Experimental characterization of the degradation modes in End of Life samples thought the carried out tests;
    - Development/adaptation of physical model to support the interpretation of degradation modes;
- Modelling and measure the behaviour of a set of heterogeneously aged cells in parallel configuration as a first step towards the understanding of module testing methods.

3. Methodology

3.1. Battery samples

The LIB samples used in this thesis work are the A123 ANR26650 M1A and the A123 ANR26650 M1B. Their main characteristics are listed in *Table 1* and are taken from the corresponding datasheets [1, 2]. They correspond to the same category of batteries but model M1B is the direct replacement of M1A, therefore both models were tested separately as one main difference arose. As confirmed by geometrical measurements performed on both samples, the active area of the two cells, also reported in the table below differs by $\approx 8.7\%$ which is in line with the variation in capacity $\approx 8\%$.
The samples were supplied by a private company and comprehended both new as well as aged cells which were employed in real automotive operation. Type M1B cells were the only ones available in pristine conditions and 17 of them were tested for a complete mapping of their characteristics. The other share of cells instead all experienced real life usage for hybrid automotive purposes for an interval of time between 2 to 8 years. The majority of these cells were of M1A type while only the more recent samples were M1B type. The selection of these samples will be motivated in *Section 5.1*, but overall, a total of 40 aged samples (32 M1A and 8 M1B) were tested.

Battery samples characteristics		
Manufacturer	A123	A123
Model	ANR26650 M1A	ANR26650 M1B
Design	Cylindrical	Cylindrical
Anode chemistry	Graphite	Graphite
Cathode chemistry	LFP	LFP
Cell Dimensions (mm)	Ø26 x 65	Ø26 x 65
Cell active area (m^2)	0.1690	0.1852
Cell Weight (g)	72	76
Cell Capacity (nominal/minimum, Ah)	2.3/2.2	2.5/2.4
Voltage (nominal minimum/maximum V)	3.3	3.3
Internal Impedance (1kHz AC typical, mΩ)	8	6
Maximum Continuous Discharge (A)	70	70
Maximum Pulse Discharge (10 seconds, A)	120	120
Operating Temperature	[-30°C; 55°C]	[-30°C; 55°C]
Storage Temperature	[-40°C; 60°C]	[-40°C; 60°C]

Table 1: *Specifics of the LIB samples involved in the project work.*

3.2. Experimental testing station

The testing station for the experimental measurements was built upon the already existing system developed during the previous thesis work [12] within the MRT Fuel Cell & Battery Laboratory. The small climatic chamber (Binder KT 53 [7]) was employed in a short calendar campaign without the need for any modifications while the big chamber (Binder MKF 720 [8]) was used as host for the enlarged testing system. The improvements consisted in the implementation of four additional channels for battery testing featuring components dimensioned to withstand currents up to 100 A with respect to the 20 A limit of the previous configuration. To do so, five additional Chroma UM 63640-80-80 electronic loads [11] (one for each of the four channels plus one for current regulation on the whole branch) were added in parallel to the already available ones, requiring for a complete renovation of the circuital system of the switch box (8 x Finder 22.64) and of the acquisition boards (1 x NI cDAQ-9171, 2 x NI USB 6218). The power supply was instead provided by the same NI RMX-4124 device which had no problem in working with two parallel branches of these dimensions. Furthermore, the control system,

implemented in the software Labview, was adapted to the new configuration so that it was able to control and acquire data about the tested samples while still ensuring the observance of the operational voltage boundaries of each cell. Regarding the system's security, an Arduino Mega 2560 Rev3 was used for the implementation of a mechanical safety layer, able to stop the system if voltage limits are exceeded or if the software does not respond for a relevant period of time. Finally, to perform some high precision measurements on the batteries, an Autolab PGSTAT30 potentiostat with a FRA2 module was occasionally employed in the experimental tests. As previously mentioned, the CIRC-eV laboratory was part of this work as well, in particular it was used as an hub for the management and storage of the battery modules thanks to the presence of the appropriate Lithium-ion storage cabinets.

3.3. Experimental techniques

Within the possibilities and the limits of the experimental station, a selection of measurements have been chosen to describe the battery samples functioning and their degradation state, in correlation to the operative conditions. This comprehends charges and discharges, pulse tests and Electrochemical Impedance Spectroscopy (EIS), all evaluated at multiple conditions, briefly described in the following paragraph. Charge and discharge measurements focus on the relation between the cell voltage and the capacity exchanged during the test. Their main feature is that, being strongly influenced by the test operating conditions, allow for the understanding of all losses effects happening during the process. The two variables with the higher impact are C-rate, a dimensionless parameter defined as charge/discharge current over battery nominal capacity, and temperature. The former strongly influences kinetics as it is an indicator of how much we move away from the equilibrium condition and hence is related to higher overpotentials as the c-rate increases. The latter instead positively effects ion mobility and solid-state diffusion enhancing the battery performances given higher temperatures. For this reason "slow" discharges at conditions that dampen the previously analyzed losses effects, are widely used in literature [3, 4, 16, 18]. For the sake of this work discharge tests at C/10 and 25°C (until 2V lower voltage limit is reached) were performed for residual capacity quantification due to almost identical results respect to even slower measures like C/25, but with much less time required. Moreover, discharges at multiple c-rate and temperature combinations were performed for mapping the cell behaviour. Furthermore, the C/10 discharge was also considered as a good approximation of a close to equilibrium curve. Concerning the battery charging protocol instead, a standard procedure found in multiple literature references [4, 33–35, 57] as well as in the battery datasheets [1, 2] was used. This consisted in 1C charging rate in CC-mode followed by CV charging at 3.6 V until the 0.1 A condition was reached.

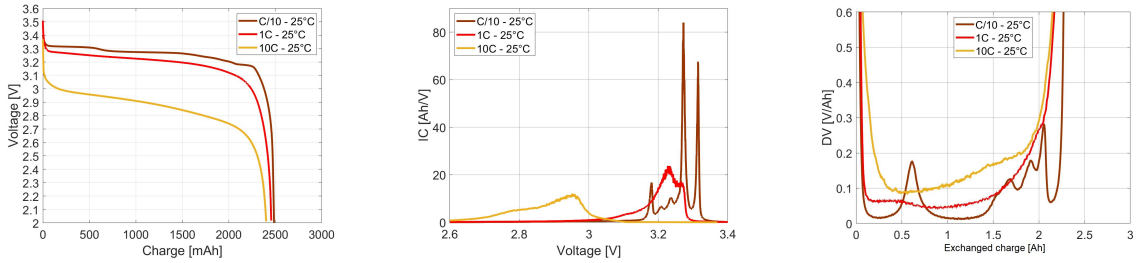

(a) *Discharge curves at 3 different C-rate values.* (b) *Incremental Capacity obtained from Eq. 3.* (c) *Differential voltage obtained from Eq. 4.*

Figure 7:

Starting from the battery charge/discharge curves, two additional diagnostic tools can be derived. The incremental capacity (IC) and differential voltage (DV) are defined as the partial derivative of exchanged charge with respect to voltage and its opposite.

$$IC = \frac{\partial Q}{\partial V} \tag{3}$$

$$DV = \frac{\partial V}{\partial Q} \tag{4}$$

Therefore, the area under the IC curve (*see Fig. 7b*) is the exchanged charge, while the one under the DV curve (*see Fig. 7c*) corresponds to the cell voltage. These two curves are able to represent the thermodynamic characteristics of the electrodes, that during the battery operation, undergo a process characterised by the alternation of single-phase regions and phase transitions (*see Section 2.1*). While in single phase regions most

of the potential steps take place, during the transitional states the electrodes' potential remains constant: the amount of Li in the host material gradually increases/decreases, but the configuration of the electrode (and so its energy state, i.e. its potential) does not change until the host material is fully saturated/empty. Moreover, the IC and DV plots contain similar information expressed in different ways. Namely, when one or both the electrodes are going through a phase transition and the voltage profile is on a plateau, a valley is displayed in the DV curve and a peak in the IC curve. On the opposite, during phase equilibrium the electrodes behave as solid solutions which translates into peaks in the DV and valleys in the IC. Furthermore, both measures are useful for assessing the degradation of batteries since the translation and the variation of intensity of the IC peaks are used to analyze the loss of active material [3, 4, 16, 18] while the variation of shapes in the DV curve add on top the effect of loss of cyclable ions [33–35, 43, 57].

The second type of experimental measurements is the pulse power test. This procedure was developed starting from existing standards for pristine batteries, namely HPPC testing [15]. Power is measured at 4 main timesteps (2s, 10s, 18s and 30s) during a constant current pulse, at a controlled temperature of 25^{o}C (power is evaluated as the product of current times cell voltage.). This procedure is then repeated in both discharge and charge for a multiple values of c-rates, in our case up to 12.5C (= 31.25A) with 2.5C steps. The resting time intervals used during the various tests are 5 min between discharge/charge and 10 min between following current steps Moreover, the pulse is stopped if the cell overcomes two voltage limits of 3.8 V during charge or 2 V during discharge. 3.8 V is selected with an additional tolerance respect to the strict 3.6 V from the datasheet [64], to allow a more flexible operation in case of peaks, even though it is not suggested. The main target of this measure is specific to the type of cells analyzed in this work, because they are an high power model [2, 64] and hence, it is of main interest to evaluate the residual power capabilities.
The last technique among the experimental tests is the electrochemical impedance spectroscopy (EIS), a tool widely studied in literature [28, 42, 49] and effectively applied in battery aging research [23, 30, 32, 41, 60] due to the multiple effects it depicts and the strong dependence on SoC and temperature. This type of measurement consists of the superimposition of a sinusoidal current I with frequency f on a steady state condition while recording the voltage response V. Then, the cell impedance is computed as the ratio of the voltage and current sinusoidal curves and is then processed through the Fast Fourier Transform (FFT), resulting in a complex number. As showed in *Figure 8* this procedure is repeated for a set of different frequencies that then generate a spectrum. This strong dependency of various phenomena inside the cell to frequency, allows to stress different mechanisms in function of their characteristic time. Four of them will be explained more in detail following the Nyquist plot of a pristine cell in *Figure 8*, which shows the negative imaginary part of the impedance response versus the real part. At very high frequencies (f $>$ 2 kHz) the inductive effect of the circuit cables, that is visible mainly as an imaginary contribution, is showed. For frequencies (2 kHz $<$ f $<$ 1 kHz) we can isolate the ohmic effect, also known as high frequency resistance (HFR), and hence give an estimation of the purely resistive effects inside the cell, excluding slower phenomena. The two following characteristics are in order the kinetic behaviour(1 kHz $<$ f $<$ 1 Hz) and diffusion one (f $<$ 1 Hz). The former is often referred as the combination between the charge transfer resistance (R_{ct}) and the double layer capacitance of the two electrolyte/electrode interfaces while the latter is represented by the Warburg impedance (R_w) and depicts all the slow effects dominated by lithium diffusion inside the cell components.

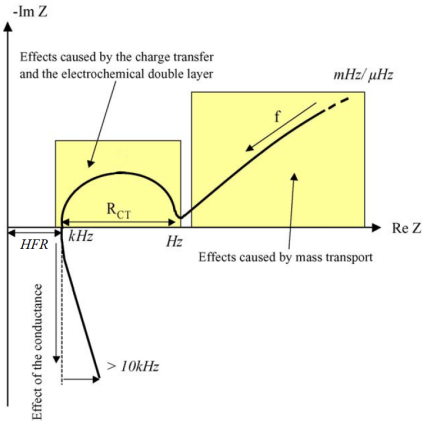

Figure 8: *Typical Nyquist plot of a Li-ion battery [32].*

3.4. Physical Model

To further interpret the experimental results, a physical based model was developed as a tool for the reproduction and description of the cells at multiple aging states, with respect to a set of characteristic parameters. The initial setting of the model was taken from the previous thesis work of the same research track [12] but it was then adapted and optimized for the specific application on LFP batteries. The model was implemented in *COMSOL Multiphysics®* following the Doyle-Fuller-Newman pseudo-two dimensional electrochemical model (P2D) (*see Fig.9a*) [31] alongside with a 2D thermal component *(see Fig.9b)* that given a heat generation term, computed by the P2D, would update the temperature distribution in the cell during a charge/discharge process. Thanks to the P2D model the physical behaviour of the battery is reproduced by means of partial differential equations (PDEs), that combine the geometrical, electrochemical and thermal properties of the cell.

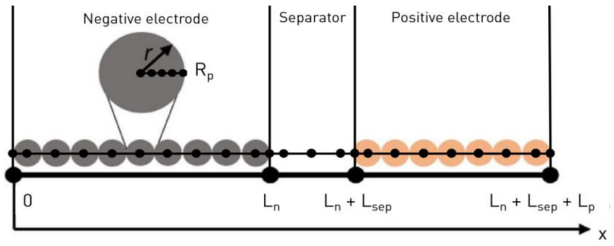

(a) *Representation of the Doyle-Fuller-Newman P2D model electrochemical domain.* [12]

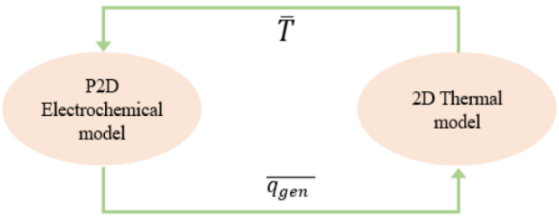

(b) *Scheme of the connection between the electrochemical and the thermal model.* [12]

Figure 9: *Li-ion battery model.*

Once the physical model was defined, an optimization algorithm was implemented alongside by Innocenti [29], as a tool for an effective calibration of the parameters that characterize the kinetic behaviour of the battery. These are listed in *Table 2* together with a specific range of variation, in which, depending on the degradation state, different combinations are allowed. For this task a Particle Swarm Optimization (PSO) algorithm [47] was chosen and implemented in *MATLAB®*. This consists in a population-based optimization tool in which the members of the population, named particles, can move in a n-dimensional space, where n is the number of parameters that has to be calibrated. There, they move driven by the minimization of an objective function defined as the difference between the experimental curve used for the calibration (either discharge curve or EIS as will be explained in the next paragraph) and the one produced by the model. To improve the exploration phase of the particles an adaptive feature [70] has been added to the algorithm by Sedzik [55], so that now, depending on the variation of an evolutionary function f, each particle has assigned one state among exploration, exploitation, convergence and jumping out and the inertia and the velocities coefficients are imposed as function of the state itself.
This configuration describes the tool and the method used for the calibration of the so called "kinetic" parameters. These are divided in two subgroups (*KIN1* and *KIN2* in *Tab.2*) which correspond to two different optimization steps that were formulated in the previous thesis work by Conti and Rondi [12] and are based on the results of an extensive sensitivity analysis of the most influential parameters of the battery model. Therefore *KIN1* parameters are calibrated on a pair of EIS curves while *KIN2* on a pair of discharge curves. This set of four curves is chosen according to the type of battery analyzed and allows for the formulation of a diagnostic protocol capable of fully describing the effect of SoC and temperature. The one adopted for this work consists in the following sequence of measurements: EIS @ (SoC = 100%, T = 25°C, f ∈ [0.02; 20000]), Discharge @ (C-rate = 10C, DoD = 50%, T = 25°C), EIS @ (SoC = 50%, T = 10°C, f ∈ [0.02; 20000]) and Discharge @ (C-rate = 1C, DoD = 50%, T = 10°C).

While for the calibration of pristine cells, the thermodynamic parameters (TDN in *Tab.2*) are kept as equal to zero, in aged cells, degradation mechanisms have to be accurately modelled in the P2D component and that is allowed by the use of measurable parameters (LLI, LAMn and LAMp *see Section 2.2*). For this purpose an additional model able to estimate those parameters was developed. Thanks to the close to the equilibrium state, of the so called slow discharge (C/10, 25°C) (*see Section 3.3*), it was possible to isolate the calibration of the thermodynamic parameters with a model that, with help of a PSO algorithm, reproduces the experimental discharge by matching the equilibrium curves of the electrodes. For a more effective calibration, IC and DV curves obtained from the slow discharge were used singularly or as a combination in a single objective function but, after some sensitivity tests, it was decided to proceed with the differential voltage curve alone. Once the thermodynamic calibration is completed, the complete calibration accounting for the kinetic parameters can be performed in the same way of the pristine cells.

	Parameter	Symbol	Value Range
KIN$_1$	Kinetic rate constant of the positive el.	k_{pos} [−]	$[5e-12\,;5e-9]$
KIN$_1$	Kinetic rate constant of the negative el.	k_{neg} [−]	$[5e-12\,;5e-9]$
KIN$_1$	Double layer of the positive el.	$C_{dl,pos}$ $[F\,m^{-2}]$	$[0.05\,;20]$
KIN$_1$	Double layer of the negative el.	$C_{dl,neg}$ $[F\,m^{-2}]$	$[0.05\,;20]$
KIN$_1$	Rate constant activation energy of the negative el.	$EA_{k,neg}$ $[J\,mol^{-1}]$	$[20000\,;60000]$
KIN$_2$	Ionic conductivity factor	cond_{el} [−]	$[0.05\,;1]$
KIN$_2$	Ionic diffusivity factor	diff_{el} [−]	$[0.05\,;1]$
KIN$_2$	Solid diffusivity of the positive el.	$D_{s,pos}$ $[m^2\,s^{-1}]$	$[5e-18\,;1e-14]$
KIN$_2$	Solid diffusivity of the negative el.	$D_{s,neg}$ $[m^2\,s^{-1}]$	$[1e-16\,;1e-13]$
TDN	Loss of Lithium Ions	LLI [−]	$[0\,;1]$
TDN	Loss of Active Material at positive el.	LAM_p [−]	$[0\,;1]$
TDN	Loss of Active Material at negative el.	LAM_n [−]	$[0\,;1]$

Table 2: *Parameters for model calibration with their relative ranges of variability.*

4. BoL samples

4.1. Experimental testing

The first step in the experimental campaign consisted in the characterization of the Beginning of Life (BoL) cells. This was adopted as a benchmark test for the End of Life (EoL) samples performance evaluation. The experimental diagnostic methodology was adapted from previous thesis works [12] to the specific samples involved in the research, but still, all of the aforementioned measurements (*see Section 3.3*) like capacity tests, discharges at various c-rates and temperatures, pulse power tests and electrochemical impedance spectroscopy analysis (EIS) were performed. These experimental measurements were then fed to the PSO algorithm (*see Section 3.4*) to obtain a description of the pristine cells that included information about kinetic parameters. Unfortunately, the only BoL samples available for the experimental testing were M1B type. Hence, it was necessary to take from literature experimental discharge curves and EIS spectra of BoL M1A type cells [3, 4, 35, 48].

The nominal cell capacity was the first feature to be measured, estimated from a full discharge curve at controlled environmental temperature of 25^{o}C and at a constant current of 0.25A (M1B nominal 0.1C C-rate). This measure was replicated on multiple samples to prove its repeatability and resulted in a maximum variation of less than 0.5%. On average, cell M1B showed a capacity of 2.488 Ah, which is in accordance with the data from the latest datasheets (2.5 Ah) [2, 64] while, from a slow discharge at C/25 (*see Fig. 10a*) performed by Dubarry *et al.* [4], cell M1A displayed a capacity of 2.240 Ah which is similar to the nominal value of 2.3Ah [1].

IC and DV curves of the corresponding discharges have been obtained mathematically for cell M1B while, curves derived from slow discharges at C/5 [3, 4, 35, 53] have been used as a reference for cell M1A (*see Fig. 10b, 10c*). The analysis of these two curves allowed for a better comparison of the processes happening during the discharge in the two cells (*see Fig. 10a*). From the DV plot it is clear that the main phenomena (which are almost entirely related to graphite) happen in a similar way in both cases with a difference in dimension of the voltage plateaus due to design differences in the two battery models (*see Section 3.1*). From the IC figure instead, it is clear that both cells go through the five main phase transition phenomena of the graphite electrode, each represented by a peak. Moreover, the slight misalignment between the two curves and the difference in peaks height are related to both differences in design and by the higher current rate used for M1A cell test (C/5 instead of C/10) which causes higher over potentials and hence, a less clear highlight of the peaks, especially at low voltage. Both IC and DV will become useful tools for assessing degradation modes by analyzing the variation of the curves' main features. In particular, each plateau of the DV curve will shrink, meaning an overall reduction in residual capacity that is differently distributed among each stage of the lithium intercalation process, which can be traced back to multiple causes. Peaks in the IC curve instead, will reduce their height due to shorter

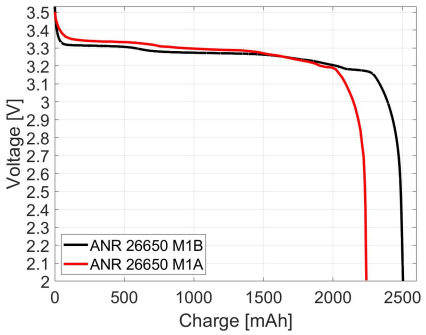

(a) *Slow discharges at C/10 for cell M1B and C/25 for M1A [4].*

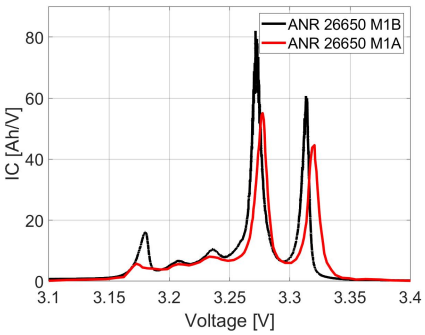

(b) *Incremental capacity curves taken from the experimental discharge for the cell M1B and from a C/5 discharge for cell M1A [53].*

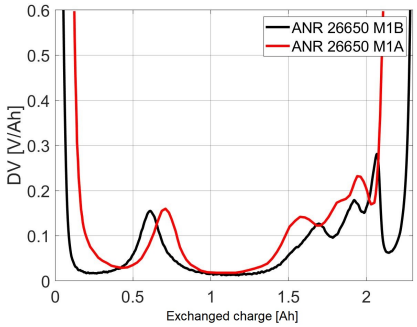

(c) *Differential voltage curves taken from the experimental discharge for the cell M1B and from a C/5 discharge for cell M1A [54].*

Figure 10: *Main curves representative of differences between the two battery models taken into account, namely ANR26650 M1A and M1B.*

voltage plateau (similarly to what showed in DV) and will likely shift towards lower voltages due to increased internal resistances of the battery (usually related to SEI growth).
After the nominal capacity test, the behavior of BoL cells at different discharge current rates was evaluated. 10C was selected as the maximum value, since the analysis of diagnostic data (*see Chap. 5.1*) highlighted that the cells usually operated within ±8C. Clearly, the higher the C-rate, the higher the overpotentials (lower voltage in discharge, opposite in charge), but also the lower the available energy and capacity, which is clear if we compare the two extreme cases of *Figure 11a*. Concerning the temperature effects, three different temperatures were applied at three different current levels, namely 0.1C, 1C and 10C at 10°C, 25°C and 40°C. Accordingly to theory, the higher the temperature, the higher the energy and capacity exchanged due to improved materials properties and improved kinetics of the reactions. Concerning cell M1A, due to the lack of BoL samples, a series of discharge curves at different C-rates in the range from C/4 to 8C was taken from the work by Prada *et al.* [48], while temperature effects were measured in the work by Li *et al.* [38] where discharges (1C) at -20°C, 0°C, 25°C and 45°C were performed. This curves showed the same response to variable conditions and hence, no additional observations are required.

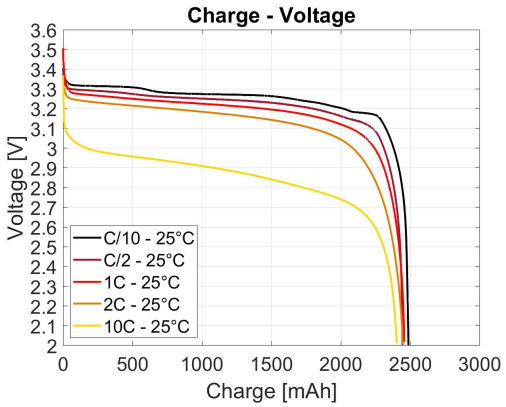

(a) *Experimental discharge curves at 10C, 2C, 1C, C/2 and C/10 of cell M1B.*

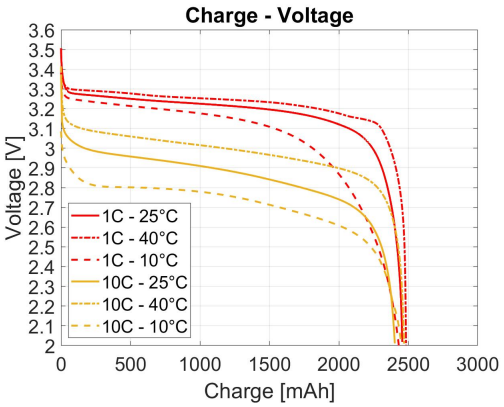

(b) *Experimental discharge curves at 10C, 1C combined with temperatures of 10°C, 25°C and 40°C of cell M1B.*

Figure 11: *Main curves representative of C-rate and temperature effects.*

The second type of measurement consisted in power pulse tests, which were carried out following the previously described guidelines (*see Section 3.3*). The power measures provided in *Tab. 3*, gather both discharge and charge pulses at five different C-rates. As evident, the larger the current, the larger the power, with values that are relatively homogeneous in time. Exceptions occur only at high discharge rates (mainly 10C and 12.5C in discharge), where the SoC variations become relevant. For repeatability confirmation the standard deviations at the measurement points were calculated resulting in very limited variations, especially at low C-rates. While these experimental measures were taken for cell M1B, nothing was found in literature concerning pulse tests with M1A cells and for this reason ageing comparisons will be only based on M1B cells results.

Applied load - Nominal C-rate (total current)	Discharge pulse								Charge Pulse							
	Mean value [W]				DEVST [W]				Mean value [W]				DEVST [W]			
	Time after start of pulse								Time after start of pulse							
	2 [s]	10 [s]	18 [s]	30 [s]	2 [s]	10 [s]	18 [s]	30 [s]	2 [s]	10 [s]	18 [s]	30 [s]	2 [s]	10 [s]	18 [s]	30 [s]
2.5C (6.25A)	-20.1	-20.0	-19.9	-19.8	0.0	0.0	0.0	0.0	20.9	21.1	21.1	21.2	0.0	0.0	0.0	0.0
5C (12.5A)	-39.5	-39.0	-38.7	-38.4	0.0	0.1	0.1	0.1	42.6	43.0	43.1	43.2	0.1	0.0	0.0	0.0
7.5C (18.75A)	-58.2	-57.4	-56.8	-56.1	0.1	0.2	0.2	0.2	64.9	65.5	65.8	66.0	0.1	0.1	0.1	0.1
10C (25A)	-79.1	-77.5	-76.3	-75.0	0.3	0.3	0.3	0.3	88.2	89.0	89.4	89.9	0.2	0.2	0.2	0.3
12.5C (31.25A)	-93.8	-91.6	-89.9	-87.7	0.4	0.6	0.8	0.9	111.2	112.5	113.2	113.8	0.3	0.3	0.3	0.3

Table 3: *Pulse test power measurements with standard deviations from repeatability test.*

The last measurement consisted in a series of electrochemical impedance spectroscopy (EIS) at different conditions of temperature and states of charge. These curves enabled to quantify the variation of different charge and mass transport mechanisms inside the cells given different temperature and state of charge conditions. Starting with *Figure 12*, it is clear the relevant effect that temperature has on three of the four main phenomena analyzed in *Section 3.3*, namely high frequency resistance (HFR), charge transfer resistance (R_{ct}) and mass transport (R_w). Differently, the SoC does not affect both HFR and R_{ct} but causes a worsening of the diffusion effect especially at low and high SoC values (dare indicazione su due valori ed eventualmente due parole sul plot 3D) (*see Fig. 13*).

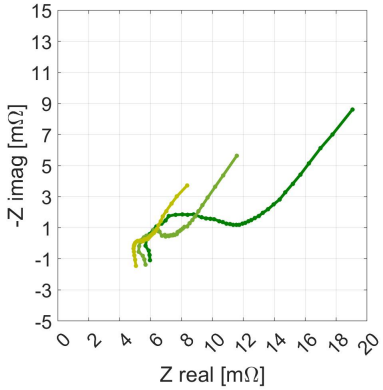

(a) *Nyquist plot of EIS at -5°C, 10°C, 25°C and 40°C.*

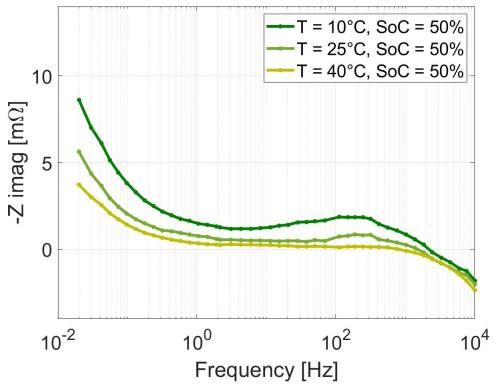

(b) *Bode plot of Imaginary axe at -5°C, 10°C, 25°C and 40°C.*

Figure 12: *Electrochemical Impedance Spectroscopy measurements of M1B Beginning of Life cell with different temperature conditions while SoC = 50%.*

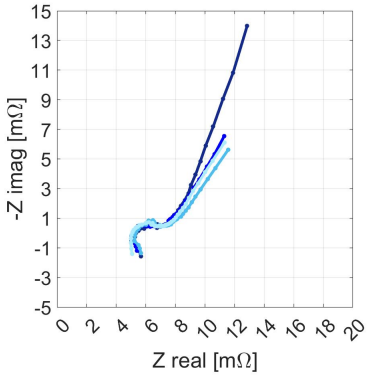

(a) *Nyquist plot of EIS at SoC = 100%, 75%, 50%, 25%.*

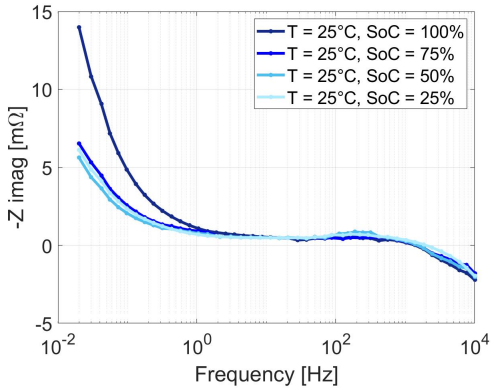

(b) *Bode plot of Imaginary component at SoC = 100%, 75%, 50%, 25%.*

Figure 13: *Electrochemical Impedance Spectroscopy measurements of M1B Beginning of Life cell with different State of Charge conditions while T = 25°C.*

4.2. Kinetic parameters calibration

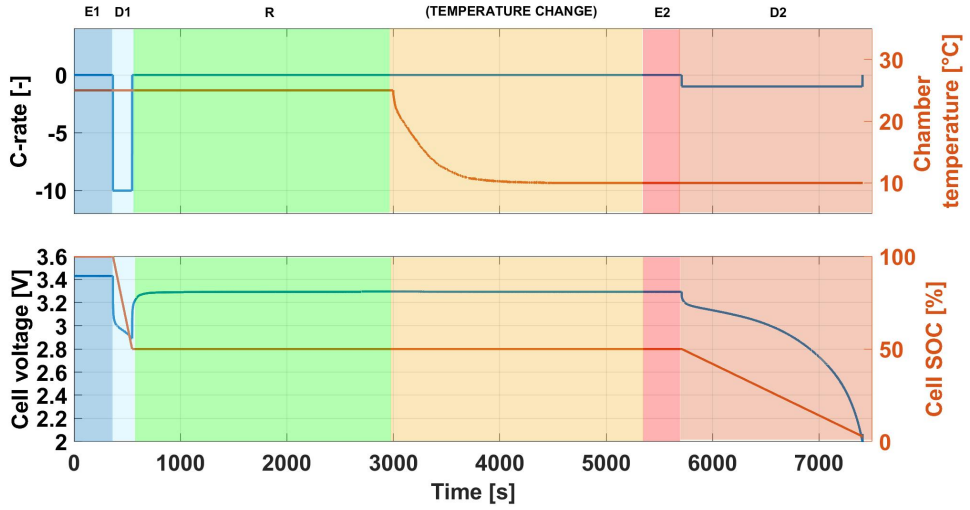

Figure 14: *Experimental protocol for kinetic parameters estimation. See Table 4 for the description of the four measurements.*

Measure	C-rate [1/h]	SoC [%]	DoD [%]	Temperature [°C]	Frequency [Hz]
EIS 1	-	100	-	25	[0.02; 20000]
Discharge 1	10	100	50	25	-
EIS 2	-	50	-	10	[0.02; 20000]
Discharge 2	1	50	50	10	-

Table 4: *Measurements for degradation diagnosis protocol.*

As previously explained in *Section 3.4*, thermodynamic parameters (LLI, LAMn, LAMp) are only related to degradation mechanisms and hence, when modelling Beginning of Life samples, are all assumed equal to zero. Therefore, once the four representative curves constituting the characterization protocol (*see Tab. 4*) were obtained experimentally, it was possible to proceed with the calibration of the kinetic parameters (*see Tab. 2*) through the calibration algorithm. A total of 125 particles were initialized in the first step (calibration on EIS curves), following a 25 particles per calibrated parameter logic, in order to start with a good amount of heterogeneous solutions. The time required for this procedure was of approximately 2 minutes per particles and hence 250 min per iteration. This meant that, if 10 iterations (good benchmark for convergence of the solution) plus initialization are considered, more than 45 hours are required for the first step only. Moreover, the second step, consisting in the calibration of 4 parameters and hence 100 particles, required approximately 1 minute per particle and hence a total of 18 hours for a 10 iteration simulation. Across the entire duration of the research project a number of simulations were performed to evaluate and correct the parameter intervals (*see Tab. 2*) and to give the right weights to the objective functions as these are not clearly defined in literature as well. Still, not all the encountered critical issues were solved. As shown in *Figure 15a*, the model was able to replicate with good approximation the discharge curves for a very wide range of C-rates (up to 10C) while many works in literature work only with much smaller ranges [10, 17, 27, 38, 39, 68, 72] or with strong assumptions like the variable radius dimension assumed per each C-rate in the work by Prada *et al.* [48]. Moreover, discharge curves as a function of temperature were well reproduced in the 10C case while the effect of temperature was underestimated in the 1C case (*see Fig. 15b*). The causes of this error could be related to the limited accuracy of the parameters for the 1C discharge which, being much less sensitive to the variation of the parameters respect the 10C discharge (enhanced kinetic effects), may be not equally optimized respect the other curve. Furthermore, EIS measurements show good dependency of temperature on the charge transfer phenomena but a bed response in terms of HFR whose variation is overestimated by the model (*see Fig. 15c*). Finally, EIS

spectra as a function of the SoC are not reported since within the range of high to mid-frequencies used for the calibration of the kinetic parameters, variations are negligible (*see Fig. 13a*).

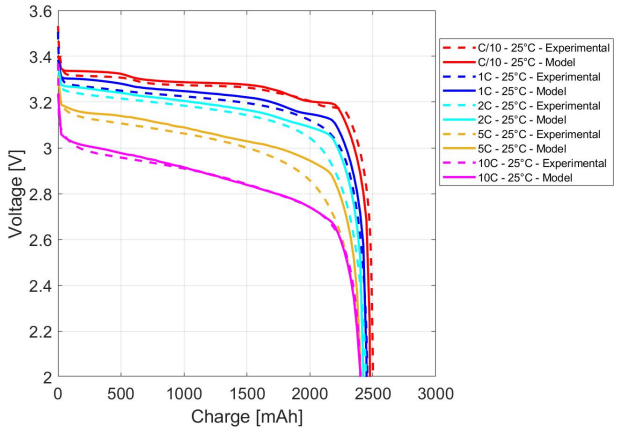

(a) *Discharge @ (C-rate = [10C, 5C, 2C, 1C, 0.1C], DoD = 100%, T = 25°C)*

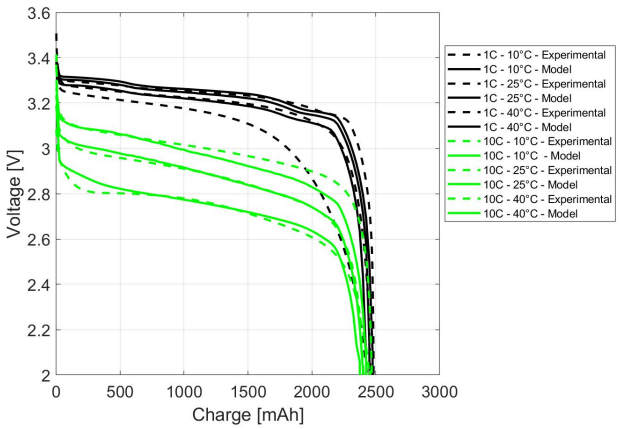

(b) *Discharge @ (C-rate = [10C, 1C], DoD = 100%, T = [10°C, 25°C, 40°C])*

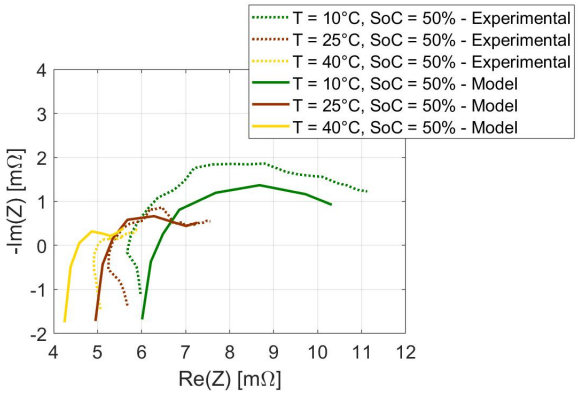

(c) *EIS @ (SoC = 50%, T = [10°C, 25°C, 40°C], $f \in [0.02; 20000]$)*

Figure 15: *EIS and discharges performed at variable conditions for model validation.*

	Parameter	Symbol	Calibrated value
KIN$_1$	Kinetic rate constant of the positive el.	k_{pos} [−]	3.67e-11
KIN$_1$	Kinetic rate constant of the negative el.	k_{neg} [−]	3.64e-09
KIN$_1$	Double layer of the positive el.	$C_{dl,pos}$ $[F\,m^{-2}]$	1.56
KIN$_1$	Double layer of the negative el.	$C_{dl,neg}$ $[F\,m^{-2}]$	0.21
KIN$_1$	Rate constant activation energy of the negative el.	$EA_{k,neg}$ $[J\,mol^{-1}]$	52562
KIN$_2$	Ionic conductivity factor	cond_{el} [−]	0.11
KIN$_2$	Ionic diffusivity factor	diff_{el} [−]	0.38
KIN$_2$	Solid diffusivity of the positive el.	$D_{s,pos}$ $[m^2\,s^{-1}]$	2.98e-17
KIN$_2$	Solid diffusivity of the negative el.	$D_{s,neg}$ $[m^2\,s^{-1}]$	1.46e-15
TDN	Loss of Lithium Ions	LLI [−]	0
TDN	Loss of Active Material at positive el.	LAM_p [−]	0
TDN	Loss of Active Material at negative el.	LAM_n [−]	0

Table 5: *Optimized parameters from BoL M1B cell calibration. For the intervals of variation see Tab. 2*

5. EoL samples

5.1. Samples selection

The samples available for the research study where chosen among three battery packs (16 modules in series), which for simplicity will be named 'A', 'B', 'C', and were supplied in modules, each made out of 96 batteries arranged as a series of 12 smaller packs (which will be named as string 1 to 12) each consisting in a parallel of 8 cells. The selection of these samples was performed accordingly to information provided by the so called LOGfiles. These are collections of diagnostic data acquired and organized by the battery management system (BMS) of each battery pack in the form of an Excel spreadsheets. The objective of this first analysis was to understand if, by gathering all the information about operating conditions, age of the samples or any other heterogeneity, it was possible to cross check this data and give an estimate of the State of Health (SoH) of the cells.
Therefore, the first step consisted in a categorisation of the modules based upon three simple indicators listed here (*see Tab. 6*):

- Year of production: gives an indication on the age of the cells involved while allows for the division into two sub-categories based on the different battery cell models. More specifically modules from 2013 are made of A123 ANR26650M1-A batteries while those from 2016 and 2018 are made of A123 ANR26650M1-B (*see Section 3.1*);

- Total amount of measurements: even though there was no confirmation upon the physical meaning of this counter between an event-based or time-based sampling, it appears from the small number of data available that the number of measurements is linearly proportional with the production year and hence can be a good indicator of the actual usage of the battery modules;

- Status assessment: information based on four colour levels (*see Tab. 6*), in order green, yellow, orange and red that indicates if there are no 'assess' conditions detected by the BMS or respectively 1, 2 or 3. Each level of the indicator is triggered when the battery string into account overcomes a set voltage thresholds for an established number of times.

Despite all the available packs were put into operation in 2013, packs 'A' and 'C' embed exclusively modules manufactured in 2018, while the third pack ('B') includes some «original» modules of the same age of the vehicle. Indeed, the largest share of modules was manufactured in 2018 while few in 2013 and only one in 2016. What is more important to notice is that the relation between age and status level is not univocal: several 2013

modules still provide no ‘assess’ status, while, at the same time, several 2018 modules do.

Module age and status	Module number	Pack 'A'	Pack 'B'	Pack 'C'
Pack number	1	2018 3.42E+07	2016 5.48E+07	2018 3.17E+07
	2	2018 3.42E+07	2018 2.78E+07	2018 3.17E+07
	3	2018 3.42E+07	2018 2.47E+07	2018 3.17E+07
	4	2018 3.42E+07	2018 4.05E+07	2018 3.17E+07
	5	2018 3.42E+07	2018 2.78E+07	2018 3.17E+07
	6	2018 3.42E+07	2013 1.01E+08	2018 3.17E+07
	7	2018 3.42E+07	2013 1.01E+08	2018 3.17E+07
	8	2018 3.42E+07	2013 9.34E+07	2018 3.17E+07
	9	2018 3.42E+07	2013 9.34E+07	2018 3.17E+07
	10	2018 3.42E+07	2013 9.34E+07	2018 3.17E+07
	11	2018 3.42E+07	2013 1.01E+08	2018 3.17E+07
	12	2018 3.42E+07	2013 9.34E+07	2018 3.17E+07
	13	2018 3.42E+07	2018 2.78E+07	2018 3.17E+07
	14	2018 3.42E+07	2013 1.01E+08	2018 3.17E+07
	15	2018 3.42E+07	2013 1.01E+08	2018 3.17E+07
	16	2018 3.42E+07	2013 1.01E+08	2018 3.17E+07

Table 6: *Modules characteristics based on: Year of production, Total amount of measurements and Status assessment.*

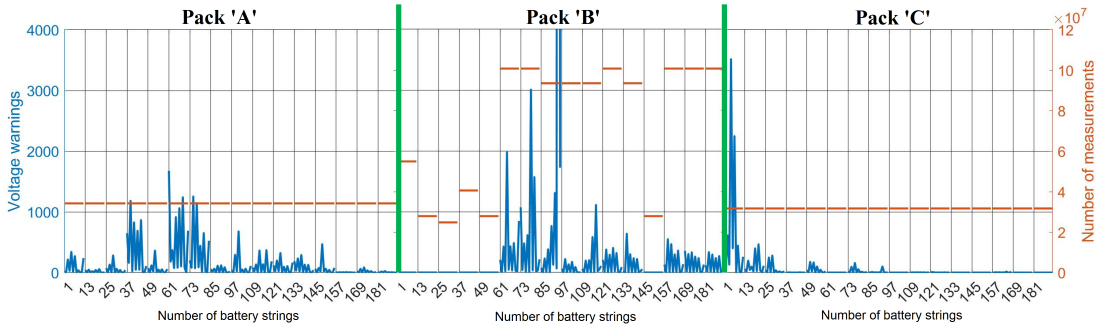

Figure 16: *Warnings count within each string, combined with the number of measurements of the corresponding module. (Each ’warning’ corresponds to a measurement taken outside the voltage limits (< 2.0 or > 3.8)*

In *Figure 16* the x-axis reports each string constituting the modules of the 3 battery packs that are available for experimental activities (packs are separated with green bars) while on the y axis two different indicators are combined. On the right, the total number of sampled measurements is reported, highlighting again that all the modules in packs ’A’ and ’C’ were completely replaced in 2018, while pack ’B’ has a more miscellaneous constitution. On the left y-axis instead, the count of total warnings defined as the cumulative number of voltage measurements outside of the recommended working range, which in this case was considered to be less than 2V and more than 3.8V. A higher number of «warnings» is expected to potentially indicate a lower state of health of the string: within the same pack and the same module as well, a very heterogeneous number of ’warnings’ is sampled, e.g. pack ’B’ and particularly module 8.

Another important information which was provided within the diagnostic data are temperature measurements. The LOGfiles contain the total amount of sampled events/time instants at a certain temperature, discretized into 5^{o}C bands. Temperature sensors are two per module and are located on the surface of two cells in the middle of the module length close to the air flow inlet and outlet, respectively. This placement, despite being rather simple, highlighted temperature differences between inlet and outlet cooling air flow and hence between a maximum and minimum value, which should be carefully considered being a potential driver of heterogeneous aging. For this purpose, an heat-map for each module’s sensor is displayed in *Figure 17a*. On the x-axis the module’s number within the pack is indicated while temperature data are reported on the y-axis and are presented as a normalized distribution over the total amount of available measurements. Temperature values occurrence is represented in the color-bar on the right: white/yellow areas correspond to the most frequent temperatures, while red/black areas correspond to temperature values which seldom occurred. In grey instead, are temperature values that were never sampled.

By analysing the charts, we can state that contrary to pack 'A', Pack 'B' and 'C' very often operated in the same temperature interval inside the range from 25°C to 35°C. Furthermore an average difference of ~ 5°C is showed between the two thermistors, suggesting an heterogeneous operation inside each module. Concerning pack 1307, the difference between T1 and T2 is confirmed, but, differently from the other two packs, the average temperature is lower and data are more dispersed over different temperature bands; it might be related to a different geographical area of operation or to an erroneous sampling. This could be investigated as it may have relevant effects on battery ageing. Finally, temperature heterogeneity is present between adjacent modules as well, but with a complex pattern, roughly showing a correlation with module age. One example are modules 1-5 and 6-8 of pack 1312C: in T2 chart, the former group (in operation since 2018) operate mostly in the 30°C-35°C band, while the latter (2013) mostly in the 35°C-40°C band.

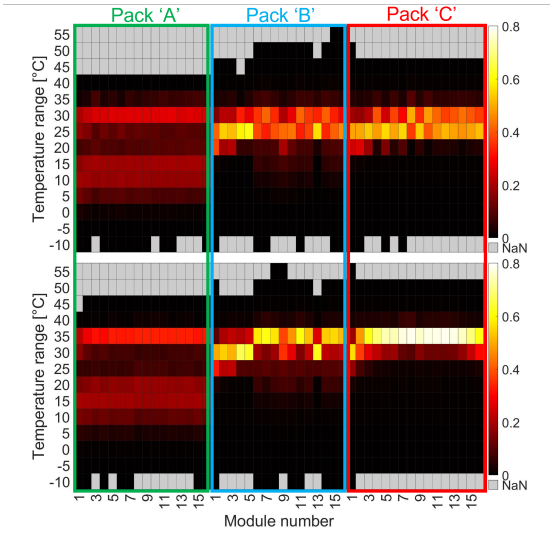

(a) *Temperature measurements heat-map. Upper group correspond to the thermistor at the inlet air flow (bottom).*

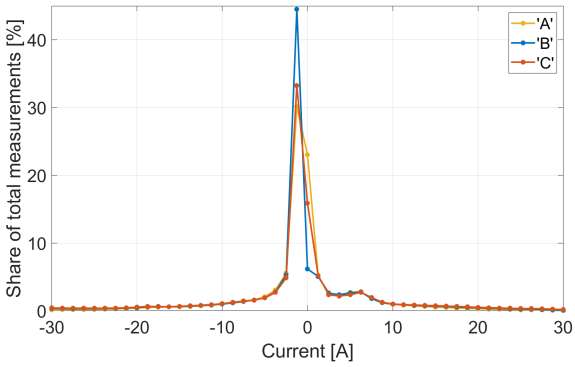

(b) *Current measurements during operation under the assumption of uniform current distribution among cells constituting the same parallel group. (Negative values are assumed as charge phase of the battery)*

Figure 17

The last useful measurement found in the LOGfiles is the pack load current, which is independent on single modules and therefore, refers to the totality of measurements taken from 2013. This value was scaled down to a single cell level with the assumption of uniform distribution of current inside each cell of the strings. Then, in *Figure 17b* the cell current probability distribution between the three packs is depicted, as the ratio of total events/time instants at that current over total number of measurements. Interestingly, the three distributions are rather consistent and show that the packs operate more frequently at currents below |20 A| (C-rate $\approx$ 8C). Beneath several discontinuity in current frequency distribution, discharge current show a highly recurrent discontinuity peak ($\approx$ 3%) at about 6.25 A ($\approx$ 2.5C), while charge current shows the highest value ($>$ 30 %) peak at (-)1.25 A ($\approx$ 0.5C), indicating two widely occurring operating conditions probably related to vehicle acceleration and battery regeneration, respectively. Very high charge and discharge current ($>$ |20 A|), still present, appear as extremely rare ($<$ 0.5 % each).
Unfortunately, more qualitative evaluations were not possible due to the lack of time references to the measurements, which could have allowed further analysis on the evolution of performances and behaviour of the cells with ageing. Therefore, in the absence of additional information, these indicators have been considered representative of the real operation and have been taken into account for the battery performance characterization.

Following the comparison among all the different modules in *Figure 6, 17* the decision was to start and eventually focus the experimental campaign on a module which could highlight multiple effects. For this reason module 8 of pack 'B' was chosen as a representative case of 2013 cells with the advantage of being made up of strings with a wide variety of number of warnings (*see Figure 16, strings from 85 to 97*).

5.2. Experimental testing - Pack 'B' Module 8 String 12

String 12 of Module 8 from pack 'B' was chosen as the most representative 2013 aged sample due to the high number of "warnings" (1724) that still did not show any sign of failure like in the case of string 11 of the same

module (all 8 cells analyzed), which was promptly discarded after slow discharge tests showed a residual capacity of less than 10% on each cell (number of 'warnings' = 110942, 2 OM more than second worst case). Moreover, every cell within each string was numbered after its relative position in the module, like showed in *Figure 18b*, where the vertical flow of cooling air is indicated. Therefore, the first indication on the degradation state of the string was given by the same residual capacity measurements (*see Fig. 18a*), resulting in an unexpected heterogeneous distribution of performances, ranging from 55% to 78% with respect to the nominal 2.3 Ah. Furthermore, better residual capacities were found in cells positioned in the lower ranks of the module (Number 5, 6, 7, 8 in *Fig. 18b*). Moreover, as the cooling system provided air from below, this effect could have been caused by an uneven temperature distribution in the vertical direction, as furtherly suggested by measurements previously analyzed in *Section 3.1*.

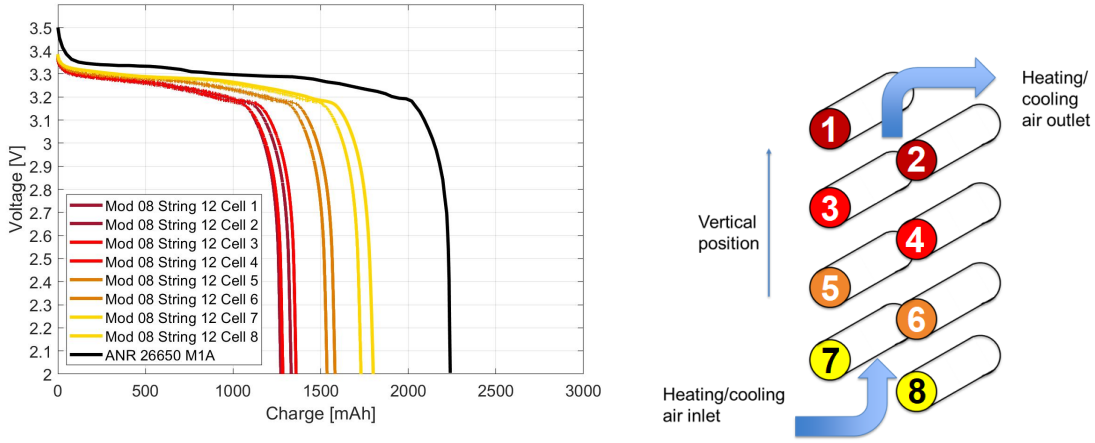

(a) *Discharge at 0.1C, 25°C for the capacity retention test.* (b) *Numeration logic of each parallel of cells (also called string).*

Figure 18

IC and DV curves were obtained from slow discharges as a tool for highlighting the thermodynamic characteristics of the electrodes and hence providing insights into degradation phenomena. *Figure 19* shows a comparison of all the 8 cells of the string plus a M1A cell in pristine conditions. Differential voltage curves (*see Fig. 19b*) highlight a mismatch between pristine and aged cells related to the almost complete loss of the first valley (every cell except number 7 and 8) and to the shrinking of the second one. This demonstrates a degradation effect on stages 1 and 2 of the graphite electrode, which is strongly related the residual capacity of each cell. As stated in the works by Li *et al.* [33–37] and in the works by Sarasketa-Zabala *et al.* [53, 54], occupation of stages 2 and 3 sites is thermodynamically favoured respect stage 1. Therefore, during a (dis)charging process the reduction of the first voltage plateau must be attributed to LLI which is often caused by SEI formation. On the other hand, reductions in stages 2 and 3 cannot be explained solely by the same mechanism. Thus, apart from the reduction of active lithium, graphite active material was apparently modified, as showed up by the peak shifting effect in stage 3. This peak gradually moves to the right as we consider more degraded batteries, meaning that less charge is stored and hence an higher LAM could be found (numerical evaluation of these parameters will be carried out later in *Section 5.3*). Therefore, even though initially, LLI was the main ageing phenomenon, the performance fade of the cell was apparently caused by a combination of LLI and LAM [35, 53]. Incremental capacity curves (*see Fig. 19a*) varied accordingly to the DV curves valleys, with the first peak (related to high SoC) almost entirely disappeared, if not for the batteries placed at the bottom of the module (7 and 8) and hence, with more residual capacity. The second peak instead, shows a significant reduction respect the BoL case and indicates a downward trend with ageing. Unfortunately, being the IC curve of M1A cell obtained from a C/5 discharge (*see Section 4.1*) it is not possible to compare the position of the peaks due to a difference in over-potentials, which are smaller in C/10 discharges performed for aged cells. Moreover, the same comparison can be performed on the aged cells only, revealing a peak shifting effect towards lower voltages with ageing, thus giving an indication on the increase of internal resistances [3, 4]. Overall, there seem to be strong similarities between the cells, a symptom that they are seemingly experiencing the same type of degradation, but only at different stages, perhaps due to non-homogeneous thermal management. Furthermore, there is certainly evidence of strong LLI, probably due to the growth of the SEI, and damage to the negative electrode while cells with worse performances display limited additional effects accountable to LAM. Therefore, these different degradation states could be assumed as subsequent steps of the same ageing process which are enhanced in cells where thermal management is less effective. These hypothesis will be furtherly evaluated in Section 5.3, where numerical values for these three parameters will be found.

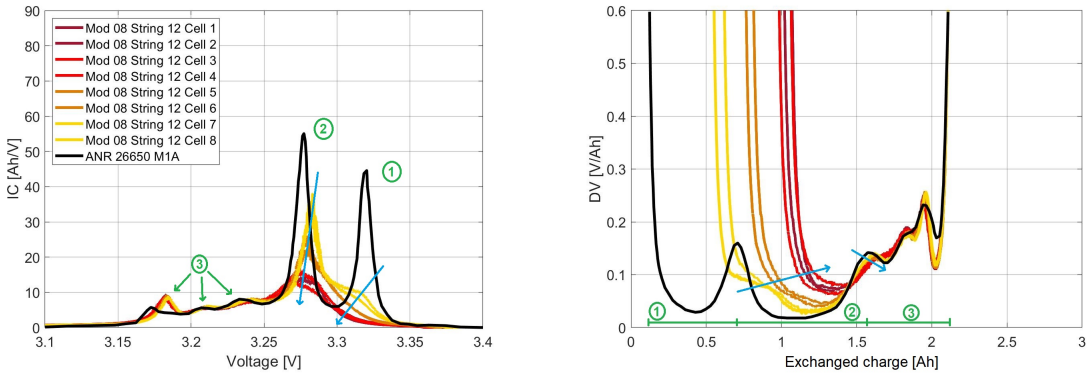

(a) *Incremental capacity* (b) *Differential voltage*

Figure 19: *Incremental Capacity (IC) and Differential Voltage (DV) from discharge at 0.1C, 25°C of string 12 module 8 compared with M1A BoL case taken from C/5, 25°C discharge in [53, 54]. Differential voltage curves are aligned with respect to last valley.*

From IC and DV curves analysis, however, it is not possible to identify the effects responsible for impedance changes. For this reason, EIS spectra measurements are reported in *Figure 20*, where both Nyquist plot (a) and Bode plot of the imaginary component (b) are presented. Even though, most of the degradation mechanisms are not uniquely assigned to a specific region of the impedance curve [30], it was possible to observe and justify many phenomena in accordance to reviewed literature. As expected, all EIS measurements showed higher impedances in all the aged cells with respect to the new ones at the same operating conditions (SoC 100%, 25°C). It is worth mentioning that, from the datasheets [1, 2], impedance of M1A cells at 1kHz (approximately the HFR value) is 8 mΩ, while for M1B model is 6 mΩ. Therefore, all cells show a pure resistive increase even though, in some cases, it is almost negligible respect to the pristine M1A cell. Accordingly to Sarasketa-Zabala *et al.* [52–54], as well as other works in literature [30, 60] an higher HFR indicates degradation of electrolyte that leads to growth of SEI layer. In the mid-frequency region, where a clear growth of the semicircle is displayed, the worsening of the kinetics of the charge transfer is often considered as the main phenomena. Moreover, from the work by Iurilli *et al.* [30], where a comprehensive review on the use of EIS is presented, many causes are implied behind the growth of the mid-frequency arch. Namely SEI growth and degradation which account for LLI [54, 73], Graphite degradation linked to LAMn [25] and finally Cathode Electrolyte Interface (CEI) formation and electrode particle cracking accounting for LAMp [41, 73]. Concerning low-frequencies instead, effects are very limited as the diffusion branch is often solely shifted towards the right due to the combined effects of the previously analyzed phenomena. Therefore, cathode particle cracking and structural disordering, which[30] should be the main degradation phenomena in this region, have been neglected in further analysis.

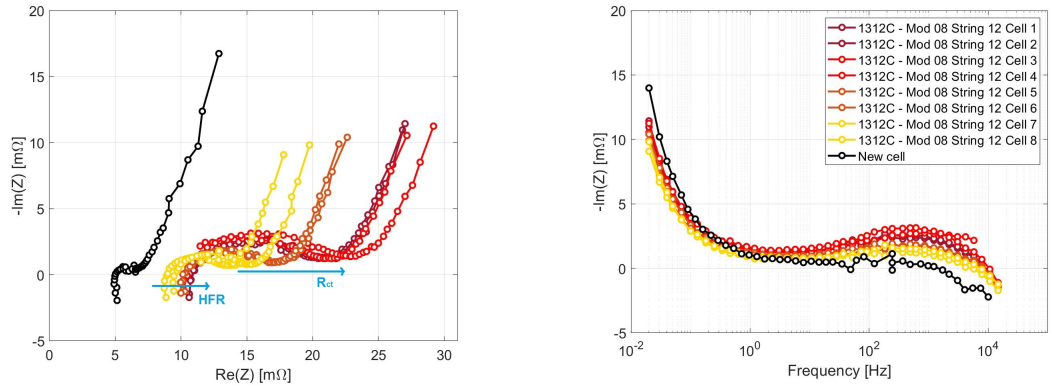

(a) *Nyquist plot.* (b) *Bode plot of the Imaginary component.*

Figure 20: *Electrochemical Impedance Spectroscopy test at SoC = 100%, 25°C.*

Finally, the residual power test, more significant from a real application point of view, showed very good residual performances in the discharge phase. All the cells were capable of providing 10C or 12.5C in discharge for 30s.

Differently, during charge phase many cells were not able to stay below the recommended voltage threshold (which was raised to 3.8 V) but as 10C charge condition occured seldom (*see Section 5.1*) the measure was kept as an indication only for comparison with other similar cells. Additionally, *Table 7* reports the power value of all the cells at 25A (10C) after 10s for both charge/discharge as well as the comparison with the BoL M1B cells. These results confirm the good performances, that seem promising for second life applications. Anyway, as this is not the main focus of the research work, batteries second life will not be treated. Finally, the same effect of the vertical positioning of the cells is found from this measure.

Mod 08 String 12	Power @10s, 10C [W]	Relative power [%]
Cell 1	-64.02	82.62
Cell 2	-62.50	80.65
Cell 3	-63.50	81.95
Cell 4	-61.09	78.84
Cell 5	-67.27	86.81
Cell 6	-67.18	86.70
Cell 7	-69.81	90.10
Cell 8	-68.87	88.89

(a) *Dischage power pulse.*

Mod 08 String 12	Power @10s, 10C [W]	Relative power [%]
Cell 1	94.83	106.54
Cell 2	95.79	107.62
Cell 3*	94.99	106.72
Cell 4*	95.41	107.19
Cell 5	95.23	106.99
Cell 6	94.93	106.66
Cell 7	92.99	104.47
Cell 8	94.28	105.92

(b) *Charge power pulse.*

Table 7: *Pulse power test measures at 10C after 10s and relative value respect the BoL M1B cell. (*) Battery reached the 3.8 V threshold before 10s hence 2s measurement is displayed.*

5.3. Thermodynamic parameters calibration - Pack 'B' Module 8 String 12

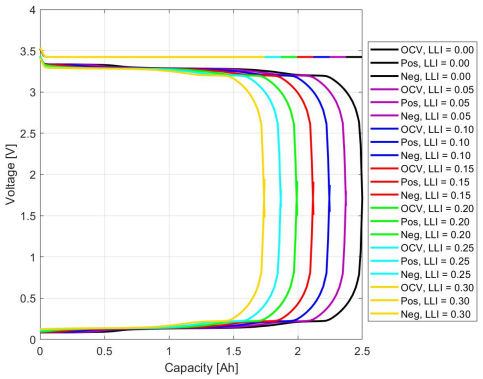

(a) *LLI sensitivity analysis with variation from 0 to 30%.*

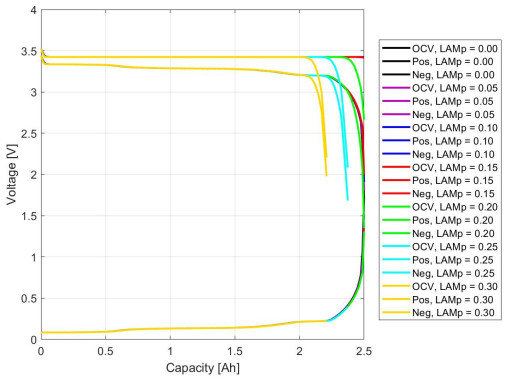

(b) *LAMp sensitivity analysis with variation from 0 to 30%..*

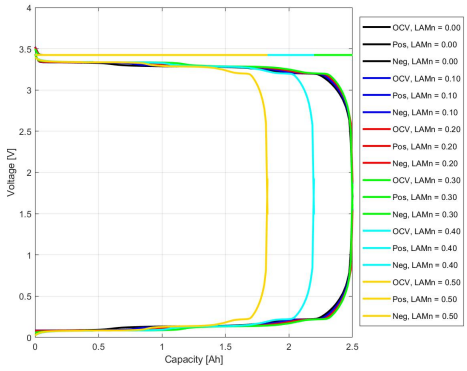

(c) *LAMn sensitivity analysis with variation from 0 to 50%.*

Figure 21: *Sensitivity analysis of TDN parameters. Each figure displays the potential of both electrodes and the OCV curve.*

Once completed the experimental campaign, it was time for the coupling with the computational modelling approach. Therefore, the first step, as previously explained in *Section 3.4* was the calibration of the thermodynamic parameters, namely LLI, LAMn, LAMp. The optimization process was performed upon the slow discharge curves (0.1C, 25°C) (see Fig. 18a), which are assumed to be in close-to-equilibrium state, and hence not affected by kinetic effects. To better understand the influence of these parameters on the OCV curve, a sensitivity analysis has been performed, changing one parameter at a time and simulating the aforementioned slow discharges. The effect of LLI is mainly impactful from a residual capacity point of view while both electrodes physical properties are unchanged. This translates in shifted electrodes equilibrium curves (*see Fig. 21a*), as a gradually lower lithium concentration is found in the electrodes, with respect to the begin of life case, while still ensuring the same starting OCV value. When LAM occurs instead, the electrode involved in the degradation decreases its ability to accept intercalating ions and thus, it behaves as a smaller electrode. This results in a shrinkage of the equilibrium curve of the electrode affected by LAM. The impact this phenomena has on the positive and on the negative sides is fairly different due to the shapes of their intercalation curves. On the positive side there is no visible effect for losses below $\approx 20\%$ (*see Fig. 21b*). Indeed, since at SoC $= 0\%$ the maximum concentration of the positive electrode (BoL conditions) is $\approx 70\%$ and being the equilibrium potential of $LiFePO_4$ completely flat up to $\approx 90\%$ [22, 58], a reduction higher than $\approx 20\%$ is required. On the other hand, on the negative side shrinkage of the equilibrium curve is immediately visible (*see Fig. 21c*) as phase changes are gradually shifted towards the right until the electrode dimension becomes limiting and the OCV curve starts to get shorter (LAMn $> 40\%$).

Thus, multiple sets of parameters, each able to reproduce the corresponding experimental curve (*see Fig. 22*), were obtained as showed in *Table 8*. The interpretation of the results allowed for a preliminary quantification of the weights that each degradation phenomena has. Therefore, it was immediately clear that while LLI and LAMn vary accordingly to the experimental measurements results, LAMp has a limited effect that is not quantifiable from these curves, as expected by the sensitivity analysis previously conducted (*see Fig. 21b*). Thus, only LLI and LAMn were furtherly evaluated.

Module 8 String 12	Residual capacity		LLI	LAMp	LAMn	LAMn/LLI
	[mAh]	[%]				
1	1272	55.3	0.439	0.032	0.308	0.701
2	1332	57.9	0.418	0.209	0.279	0.669
3	1360	59.1	0.401	0.013	0.262	0.653
4	1284	55.8	0.433	0.000	0.305	0.704
5	1537	66.8	0.331	0.173	0.169	0.510
6	1582	68.8	0.305	0.001	0.142	0.466
7	1800	78.3	0.207	0.065	0.006	0.031
8	1730	75.2	0.241	0.132	0.059	0.245

Table 8: *Thermodynamic parameters calibrated for cells of string 12 Module 8. (Each parameter has its own color scale with green always referring to better performances and hence, less degradation; nothing was used for LAMn as this parameter does not follow any logic for small values)*

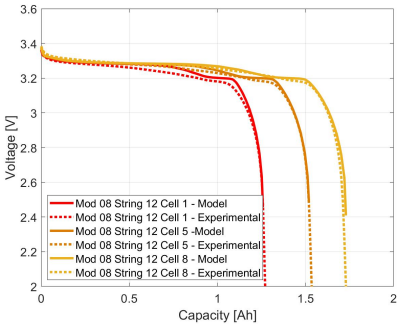

Figure 22: *Validation of thermodynamic parameters calibration results on slow discharge curves (0.1C, 25°C).*

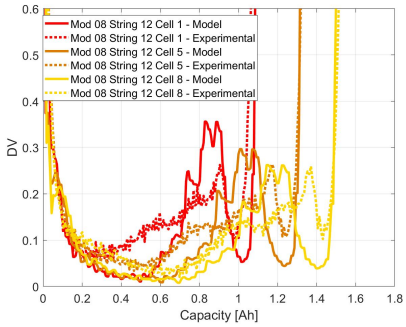

Figure 23: *Validation of thermodynamic parameters calibration results on Differential Voltage curves.*

In accordance to the works by Sarasketa-Zabala *et al.* [53, 54], it was found that while both parameters increase as the residual capacity is reduced, the relative weight of LAMn over LLI is not constant, with the former indicator growing more than the latter (*see LAMn/LLI in Tab. 8*). This could indicate that due to different operating conditions or to a more advanced degradation state, at some point the dominant degradation mechanism changes from solely LLI to a combination of LLI and LAM. A similar result is obtained by Dubarry *et al.* in [3, 4] where, by performing dynamic stress tests to a set of LFP batteries, a recurring inflection point, after which degradation significantly increased, was found. LAMn was identified as the major contributor of this phenomena while lithium plating was accounted as the underlying aging mode inducing it.

5.4. Comparison with experimental tests on additional cells

The experimental testing was not limited to an 8 cells sample, while up to 40 cells were tested throughout the entire campaign. At first String 02 of Module 8 was chosen as a direct comparison to String 12, since, being

on the same module, both had same operational conditions.The only difference between the two, which was of interest for the understanding of the significance of the LOGfiles, was the number of 'warnings' detected by the BMS while. Zero for String 02 while 1724 for String 12. Thus, the same set of measurements were taken, resulting in a moderately different aging of the cells, especially if looking at the vertical regression of performances (*see Fig. 9a*). Indeed, while the cells on the low ranks were found with similar residual capacities and power respect those of String 12, those on the high ranks showed better performances. As shown in *Table 9a*, the four bottom cells of String 02 are comparable with cells 7 and 8 of String 12 while, the top four are comparable with cells 5 and 6. Similar results were found from the pulse power tests and the EIS measurements (*see Tab. 9b, 9c*). However, from measures on single cells, it was not possible to understand if the number of 'warnings' detected was a cause or an effect of the different degradation state of the cells in the two different strings. Finally, thermodynamic parameters calibration showed results in accordance with those of string 12 (*see Tab. 9d*), therefore, no additional considerations are added.

Residual Capacity	Mod 8 String 2	
	[mAh]	[%]
Cell 1	1584	68.9
Cell 2	1589	69.1
Cell 3	1631	70.9
Cell 4	1542	67.0
Cell 5	1807	78.6
Cell 6	1772	77.0
Cell 7	1841	80.0
Cell 8	1808	78.6

Residual Capacity	Mod 8 String 12	
	[mAh]	[%]
Cell 1	1272	55.3
Cell 2	1332	57.9
Cell 3	1360	59.1
Cell 4	1284	55.8
Cell 5	1537	66.8
Cell 6	1582	68.8
Cell 7	1800	78.3
Cell 8	1730	75.2

(a) *Residual capacities of both strings 02 and 12. The value in percentage is relative to the nominal capacity of 2.3Ah of a M1A pristine.*

Mod 08 String 02	Power @10s, 10C [W]	Relative power [%]
Cell 1	-67.66	87.33
Cell 2	-67.75	87.44
Cell 3	-67.98	87.73
Cell 4	-66.90	86.34
Cell 5	-68.77	88.75
Cell 6	-69.39	89.56
Cell 7	-70.16	90.55
Cell 8	-70.24	90.65

(b) *Discharge power pulse test on string 02. For comparison with String 12 see Figure 7a.*

	A0802		
	[mAh]	R_Ω	R_CT
Battery 1	1584	9.47	5.93
Battery 2	1589	9.88	6.32
Battery 3	1631	10.04	5.76
Battery 4	1542	9.75	6.65
Battery 5	1807	9.24	4.76
Battery 6	1772	9.25	4.45
Battery 8	1808	8.73	3.47
Battery 7	1841	8.44	3.96

	A0812		
	[mAh]	R_Ω	R_CT
Battery 1	1272	10.91	9.49
Battery 2	1332	10.85	10.95
Battery 3	1360	10.31	10.99
Battery 4	1284	10.50	12.30
Battery 5	1537	10.27	6.93
Battery 6	1582	10.13	6.77
Battery 7	1800	8.95	4.65
Battery 8	1730	9.52	5.48

(c) *Eis parameters relative to both strings 02 and 12.*

Module 8 String 02	Residual capacity [mAh]	LLI	LAMp	LAMn	LAMn/LLI
1	1584	0.307	0.000	0.151	0.492
2	1589	0.307	0.193	0.156	0.508
3	1631	0.287	0.235	0.119	0.414
4	1542	0.324	0.000	0.168	0.517
5	1807	0.205	0.000	0.023	0.114
6	1772	0.224	0.001	0.039	0.172
7	1841	0.197	0.047	0.001	0.004
8	1808	0.211	0.074	0.018	0.086

(d) *Thermodynamic parameters calibrated for cells of string 02.*

Table 9: *Entire set of experimental measurements and calibrated model parameters characterizing String 02 of Module 08.*

Even though it was not possible to obtain a statistically significant measurement, an additional set of cells with similar diagnostic data (LOGfiles) was tested. This comprehends Cells 1-3-5-7 (taken from the same vertical line, *see Fig. 18b*), from Strings 02 and 05, within Module 06 of the same battery pack. The results obtained confirmed the differences between the case with a low number of warnings (0 for String 02) and the case with a relevant amount (1920 for String 05). Residual capacities and power pulse tests, showed consistent numbers with respect to the previous strings with a clear degradation pattern as a function of the vertical position of the cells (worse performances on the top section of the module). EIS measurements instead, displayed mixed results with higher charge transfer resistances than expected in some cells but still always in accordance with the degradation patterns previously highlighted. Thermodynamic parameters calibration as well demonstrated the consistency of the measures taken within the battery pack. Unfortunately, due to lack of 2013 modules in the other packs, it was not possible to evaluate the variability of the measures with respect to samples which went through different operational stressors (*see Fig. 17*, overall similar current rates distribution but differences in temperature measurements).

The last 8 cells to be analyzed in the campaign were taken from a module with completely different aging characteristics with respect to the previous ones. Module 1 of the same battery pack ('B') was chosen being a 2016 sample. Moreover, it has to be considered that this module comprehends only model M1B cells, and hence, an additional difference with respect to previously analyzed cells. However, experimental results showed performances much better than what expected, with residual capacities above 95% in all cases and power variations of less than 6% in discharge and less than 2% in charge. Concerning EIS measurements instead, very limited HFR increase respect the BoL case (less than 1mΩ) while slightly bigger increase in charge transfer

resistances, still in line with previously analyzed cells. Moreover, as ageing was still so limited, it was difficult to highlight any clear temperature driven degradation pattern. For the sake of completeness, a thermodynamic parameters calibration was carried out as well. This showed very limited losses, in accordance to what was expected with both LLI and LAMn always below 3%.
Finally, given the performances close to BoL of 2016 samples, it was decided to not perform any measurements on the 2018 modules but to introduce a preliminary study on the behaviour of heterogeneously aged cells in parallel configuration.

6. Tests of cells in parallel configuration

The understanding of how a parallel configuration of cells, each with a different degradation state, works, is a fundamental step towards the understanding of ageing modes evolution in time. Therefore, in this chapter some experimental measurements performed while the module was still completely intact will be analyzed while, a post-disassembly analysis of a parallel of 4 cells will be studied both experimentally as well as from a modelling point of view. The objective of this final Chapter of the thesis work is to find some relations between single cell and parallel of multiple cells measurements, in preparation for future studies on non-invasive diagnostic methods for battery modules.

EIS was performed by the Autolab potentiostat on all the strings of Module 08 as well as on a BoL one. This allowed for a direct comparison between the single cell spectra and the one of an 8 cell parallel. Moreover, it was shown that, with good approximation, it is possible to move from one measure to the other by means of a simple equivalent impedance calculation plus a concentrated purely resistive effect, likely related to the different equipments used for the two measures (one with the AutoLab potentiostat, the other with the experimental station, *see Section 3.2*). Therefore, *Figure 24a* displays the experimental EIS spectra of the entire string compared with the equivalent impedance computed as $\frac{1}{Z_{eq}} = \sum \frac{1}{Z_{cell,i}}$ while *Figure 24b* shows all the EIS spectra of the single cells along with the "equivalent cell" computed from the string measure, with the same equation as before, assuming all $Z_{cell,i}$ equal.

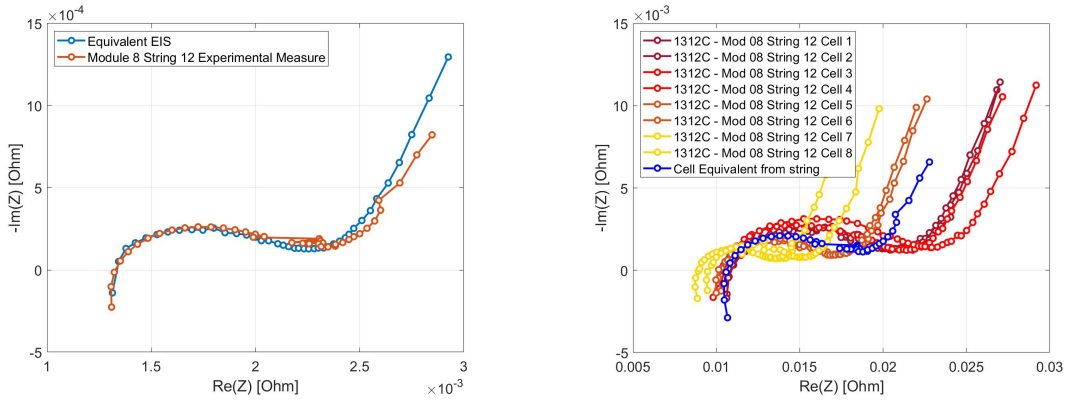

(a) (b)

Figure 24: *Example of correlations between EIS measurement on entire string 12 and single cells. (NOTE: different axis limits between the two graphs)*

The second step aimed at the reproduction of the operational functioning of a parallel of cells. This test, given a full characterization of each cell, enables the understanding of the contribution of each battery. Thereafter, a simple numerical model, accounting for charge and voltage balances across the parallel, was developed to estimate voltage and current flows in slow discharges. Experimental measurements were performed on three different configurations. First, four BoL cells were tested, then three in pristine conditions plus an aged sample (Pack 'B' Module 08 String 12 Cell 2) and finally four aged cells (Pack 'B' Module 08 String 12 Cells 2-4-6-8). The number of cells used for the parallel was limited to four, as a compromise to allow for higher current rates for pulse tests (limit of 80A per channel hence, up to overall 7.5C) while still having the possibility of taking into account the entire vertical degradation pattern within the string (more heterogeneous samples combined). The measurements taken were slow discharges at 0.1C, 25°C to evaluate residual capacity of the cells and power pulse tests at 7.5C, 25C° to evaluate possible temperature gradients differences.

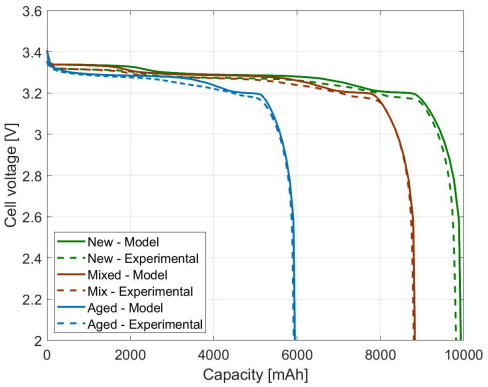

(a) *Voltage profiles of the three different configurations discharge curves at 0.1C, 25°C combined with numerical model predictions.*

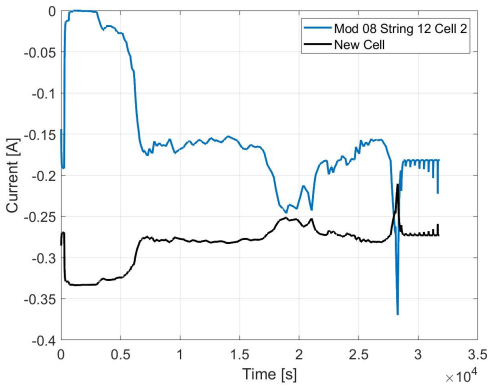

(b) *Current profile of each cell in the Mixed conditions parallel (3 BoL + P1312C M08 S12 2).*

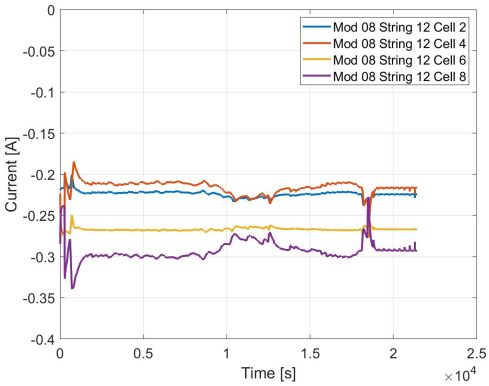

(c) *Current profile of each cell in the Aged conditions parallel (P1312C M08 S12 2-4-6-8).*

Figure 25: *Slow discharge experimental results, combined with model interpretation of current and voltage profiles.*

Figure 25a shows discharge curves of the three tested parallel configurations. The results indicate that the residual capacity is strongly influenced by the characteristics of the cells themselves and hence, with good approximation, the value obtained from this measure is representative of the sum of the single cells capacities. Moreover, currents distribute themselves during operation accordingly to *Figures 25b, 25c* where we can see that the new/less aged cells always take the biggest share of load. Overall, computing the entire charge exchanged by each battery as $I_{cell} * \Delta t/3.6$ in the "Aged" configuration, results in 1325 mAh, 1279 mAh, 1579 mAh, 1736 mAh which is in line with the residual capacities of cells 2, 4, 6 and 8 of String 12 in *Table 9a.*

Pulse test were then performed, with the main focus posed on temperature gradients as these could have been considered a proof of the model current partition.—rispiegare meglio tutta questa parte— As shown in *Figures 26a, 26b* there definitely seems to be an effect in line with what expected but, as the pulse was limited to 7.5C due to limitations of the testing station, the temperature differences are too limited to be considered a clear proof.

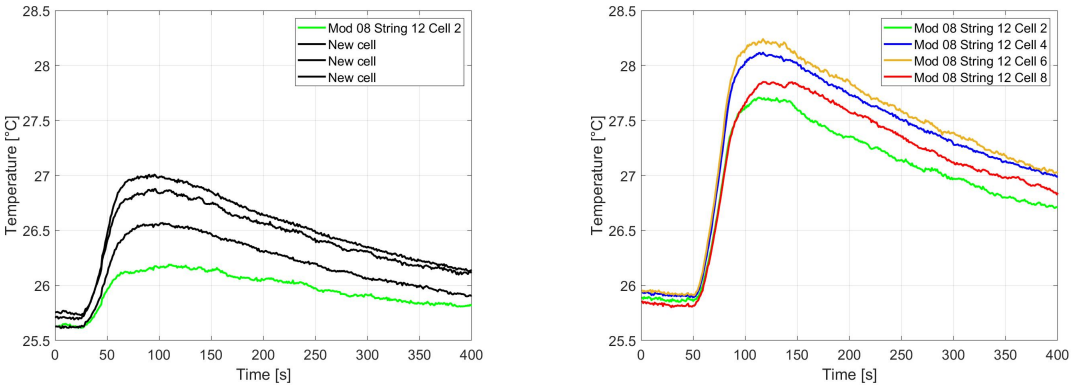

(a) *Mixed configuration temperature profiles.* (b) *Aged configuration temperature profiles.*

Figure 26: *Temperature profiles corresponding to power pulse tests at 7.5C (75A for the entire parallel), 25°C for 30s in discharge.*

7. Conclusions

This master's thesis fits into the context of the circular economy of lithium-ion batteries, acknowledging the fact that this technology has become one of the most commonly used power sources in the new generation vehicles and therefore, in the near future there will be a continuously increasing number of aged LIBs retired from that application. Moreover, stakeholders have become more confident that giving the retired batteries a second life by reusing them in less-demanding applications, such as stationary energy storage, may create new value [74]. One of the enabling factors of this circular framework is to understand the batteries degradation mechanisms, its causes and to develop a reliable and standardized measurement procedure to estimate the state of health and the remaining useful lifetime. The aim of this thesis work is to understand the degradation mechanisms during real automotive operations and to identify the stressors that influence the capacity and performance fades of the battery the most. On top of that a methodology for the calibration of parameters that, thanks to a physical LIBs model's, characterize the cell both at beginning and end of life has been developed.
The main goals achieved in this project are the following:

- A thorough literature review of $LiFePO_4$ chemistry allowed for the understanding of the basic physical principles that distinguish $LiFePO_4$ from other typologies, like the intercalation process of lithium and its effect on the shape of the equilibrium potential of the electrode which consist in a wide plateau. Alongside degradation modes were studied evaluating different operational conditions that could stimulate different effects depending on the application. Therefore the most relevant ones like SEI formation and growth, cathode dissolution with subsequent iron deposition and lithium plating were taken into account with the use of the dual tank model which enables for the description of a degradation problem by only quantify LLI, LAMn and LAMp;

- The testing station was completely renovated and adapted to the new typology of batteries which required an increased size of the equipment. Moreover, the number of individually operating channels was brought from four to eight and their limit current rate was brought up to 80A each. From the modelling aspect instead the methodology for kinetic parameters calibration was adapted from the one used in the previous thesis works. For thermodynamic parameters instead, a new PSO algorithm able to quantify LLI, LAMn and LAMp by reproducing close to equilibrium curves was implemented;

- A comprehensive experimental testing campaign was carried out enabling the complete characterization of BoL cells from a variety of aspects. Namely the nominal capacity, the IC/DV curves characteristics, the power pulse response and the EIS spectra all at variable operating conditions. Thus, End of Life cells were tested alongside and described by comparison with respect to pristine ones. Residual capacity tests allowed for the understanding of a clear effect of sub optimal thermal management that, due to increasing temperatures along the vertical axis, causes heterogeneous degradation of the cells belonging to the same parallel. Moreover as this samples had suffered the same power loads, they were considered as subsequent degradation steps of the same battery and hence compared among them. DV and IC curves showed effects related to both LLI and LAM while EIS displayed worsening of the HFR and of the charge transfer phenomena;

- Starting from the experimental tests a diagnostic protocol was formulated to gather a representative set of curves to be used for the model parameters calibration. This was then exploited by the APSO algorithm to calibrate the kinetic parameters of the beginning of life cells but unfortunately due to time limitations it was not possible to extend the calibration to EoL cells. On the other hand, the three main thermodynamic parameters were obtain for all the EoL samples giving additional insights on degradation modes. In particular it was found that worse performances correspond to an increase of both LLI and LAMn but with different weights. As degradation worsen, the problem moves from being solely dependent on LLI to being driven by both LLI and LAMn. Similar effects were obtained in works by Dubarry *et al.* [3, 4] which motivated it as caused by lithium plating. On the other hand LAMp was acknowledged as negligible for values below 20% thank to a sensitivity study on the parameter;

- Lastly a deepening on the diagnostics of parallels of cells was performed as a first step towards the understanding of module testing methods. First experimental measurements on parallels confirmed that is possible to retrieve information on single cells about residual performances and impedance spectra. Moreover, only averaged values were obtained, therefore, allowing for comparison among different strings but losing the indication on the heterogeneity among the single cells within the parallel. Slow discharge measurements were then coupled with a simple model capable of reproducing the behaviour of such a configuration by balancing charges among the cells. This was used to reproduce the instantaneous current distribution of the cells which showed that the bigger share of current is always taken by less degraded cells.

Overall, the testing campaign gave a good understanding of the cells conditions after real automotive operation. This include effects already known from lab testing with the addition of some unexpected heterogeneity related to operation. Still many points remain open for further development:

- Carry out experimental measurements on cells with different operational stressors (different battery pack) to quantify the variability of the results with respect to this work;

- The kinetic parameters calibration of the EoL cells could enable for the understanding of additional phenomena happening within ageing. This results could be furtherly enhanced if the LIB model was improved on working with wide ranges of C-rate and temperature which are distinctive of $LiFePO_4$ high power cells;

- A cycling and a calendar campaign could be performed on both BoL and EoL samples. In the first case to understand if LAB induced degradation is comparable and eventually which of the two types of degradation campaigns is predominant. In the second case instead to evaluate what are the future margins of usage for second life applications;

- Finally the study the parallel configuration could be improved in many different ways:
  - Formulate a methodology for a fast but yet complete set of measurements;
  - Model the parallel configuration with a physical model instead of using concentrated resistances;
  - Find a measure able to quantify the heterogeneity of the cells within a single string.

8. Bibliography and citations

References

[1] A123. Datasheet anr26650-m1a 2011.

[2] A123. Datasheet anr26650-m1b 2011.

[3] D Anseán, M Dubarry, A Devie, BY Liaw, VM García, JC Viera, and M González. Fast charging technique for high power lifepo4 batteries: A mechanistic analysis of aging. *Journal of Power Sources*, 321:201–209, 2016.

[4] D Anseán, M Dubarry, A Devie, BY Liaw, VM García, JC Viera, and M González. Operando lithium plating quantification and early detection of a commercial lifepo4 cell cycled under dynamic driving schedule. *Journal of Power Sources*, 356:36–46, 2017.

[5] Jakob Asenbauer, Tobias Eisenmann, Matthias Kuenzel, Arefeh Kazzazi, Zhen Chen, and Dominic Bresser. The success story of graphite as a lithium-ion anode material–fundamentals, remaining challenges, and recent developments including silicon (oxide) composites. *Sustainable Energy & Fuels*, 4(11):5387–5416, 2020.

[6] Doron Aurbach, Yosef Talyosef, Boris Markovsky, Elena Markevich, Ella Zinigrad, Liraz Asraf, Joseph S Gnanaraj, and Hyeong-Jin Kim. Design of electrolyte solutions for li and li-ion batteries: a review. *Electrochimica acta*, 50(2-3):247–254, 2004.

[7] Binder. Data sheet model kt 53.

[8] Binder. Data sheet model mkf 720.

[9] Christoph R Birkl, Matthew R Roberts, Euan McTurk, Peter G Bruce, and David A Howey. Degradation diagnostics for lithium ion cells. *Journal of Power Sources*, 341:373–386, 2017.

[10] J Chiew, CS Chin, WD Toh, Z Gao, J Jia, and CZ Zhang. A pseudo three-dimensional electrochemical-thermal model of a cylindrical lifepo4/graphite battery. *Applied Thermal Engineering*, 147:450–463, 2019.

[11] chroma. Chroma 63640-80-80 load module.

[12] A. Rondi D. Conti. Experimental investigation of lithium-ion battery automotive related aging and model-based interpretation. Master's thesis, Energy Engineering, 2020-21.

[13] C Delacourt, L Laffont, R Bouchet, C Wurm, J-B Leriche, M Morcrette, J-M Tarascon, and C Masquelier. Toward understanding of electrical limitations (electronic, ionic) in limpo4 (m= fe, mn) electrode materials. *Journal of the Electrochemical Society*, 152(5):A913, 2005.

[14] Charles Delacourt, Philippe Poizot, Jean-Marie Tarascon, and Christian Masquelier. The existence of a temperature-driven solid solution in lixfepo4 for 0 x 1. *Nature materials*, 4(3):254–260, 2005.

[15] Joseph A Drallmeier, Clement Wong, Charles E Solbrig, Jason B Siegel, and Anna G Stefanopoulou. Challenges of a fast diagnostic to inform screening of retired batteries. *IFAC-PapersOnLine*, 55(24):185–190, 2022.

[16] Matthieu Dubarry and Bor Yann Liaw. Identify capacity fading mechanism in a commercial lifepo4 cell. *Journal of power sources*, 194(1):541–549, 2009.

[17] Matthieu Dubarry, Cyril Truchot, and Bor Yann Liaw. Synthesize battery degradation modes via a diagnostic and prognostic model. *Journal of power sources*, 219:204–216, 2012.

[18] Matthieu Dubarry, Cyril Truchot, and Bor Yann Liaw. Cell degradation in commercial lifepo4 cells with high-power and high-energy designs. *Journal of Power Sources*, 258:408–419, 2014.

[19] Bruce Dunn, Haresh Kamath, and Jean-Marie Tarascon. Electrical energy storage for the grid: a battery of choices. *Science*, 334(6058):928–935, 2011.

[20] Jacqueline S Edge, Simon O'Kane, Ryan Prosser, Niall D Kirkaldy, Anisha N Patel, Alastair Hales, Abir Ghosh, Weilong Ai, Jingyi Chen, Jiang Yang, et al. Lithium ion battery degradation: what you need to know. *Physical Chemistry Chemical Physics*, 23(14):8200–8221, 2021.

[21] Vinodkumar Etacheri, Rotem Marom, Ran Elazari, Gregory Salitra, and Doron Aurbach. Challenges in the development of advanced li-ion batteries: a review. *Energy & Environmental Science*, 4(9):3243–3262, 2011.

[22] Miran Gaberscek, Robert Dominko, and Janez Jamnik. The meaning of impedance measurements of lifepo4 cathodes: A linearity study. *Journal of Power Sources*, 174(2):944–948, 2007.

[23] Fei Gao and Zhiyuan Tang. Kinetic behavior of lifepo4/c cathode material for lithium-ion batteries. *Electrochimica Acta*, 53(15):5071–5075, 2008.

[24] Xuebing Han, Languang Lu, Yuejiu Zheng, Xuning Feng, Zhe Li, Jianqiu Li, and Minggao Ouyang. A review on the key issues of the lithium ion battery degradation among the whole life cycle. *ETransportation*, 1:100005, 2019.

[25] Tom Patrick Heins, Nicolas Schlüter, Sabine Teresa Ernst, and Uwe Schröder. On the interpretation of impedance spectra of large-format lithium-ion batteries and its application in aging studies. *Energy Technology*, 8(2):1900279, 2020.

[26] Michael Hess. *Kinetics and stage transitions of graphite for lithium-ion batteries*. PhD thesis, ETH Zurich, 2013.

[27] Yingxia Huang and Huanxin Lai. Effects of discharge rate on electrochemical and thermal characteristics of lifepo4/graphite battery. *Applied Thermal Engineering*, 157:113744, 2019.

[28] F Huet. A review of impedance measurements for determination of the state-of-charge or state-of-health of secondary batteries. *Journal of power sources*, 70(1):59–69, 1998.

[29] A. Innocenti. An innovative methodology to estimate the parameters of a lithium-ion battery physical model. Master's thesis, Energy Engineering, 2018-19.

[30] Pietro Iurilli, Claudio Brivio, and Vanessa Wood. On the use of electrochemical impedance spectroscopy to characterize and model the aging phenomena of lithium-ion batteries: a critical review. *Journal of Power Sources*, 505:229860, 2021.

[31] Ali Jokar, Barzin Rajabloo, Martin Désilets, and Marcel Lacroix. Review of simplified pseudo-two-dimensional models of lithium-ion batteries. *Journal of Power Sources*, 327:44–55, 2016.

[32] Andreas Jossen. Fundamentals of battery dynamics. *Journal of power sources*, 154(2):530–538, 2006.

[33] Dongjiang Li, Dmitri L Danilov, Lu Gao, Yong Yang, and Peter HL Notten. Degradation mechanisms of c6/lifepo4 batteries: experimental analyses of cycling-induced aging. *Electrochimica Acta*, 210:445–455, 2016.

[34] Dongjiang Li, Dmitri L Danilov, Lu Gao, Yong Yang, and Peter HL Notten. Degradation mechanisms of the graphite electrode in c6/lifepo4 batteries unraveled by a non-destructive approach. *Journal of The Electrochemical Society*, 163(14):A3016, 2016.

[35] Dongjiang Li, Dmitri L Danilov, Jie Xie, Luc Raijmakers, Lu Gao, Yong Yang, and Peter HL Notten. Degradation mechanisms of c6/lifepo4 batteries: experimental analyses of calendar aging. *Electrochimica Acta*, 190:1124–1133, 2016.

[36] Dongjiang Li, Dmitri L Danilov, Barbara Zwikirsch, Maximilian Fichtner, Yong Yang, Rüdiger-A Eichel, and Peter HL Notten. Modeling the degradation mechanisms of c6/lifepo4 batteries. *Journal of power sources*, 375:106–117, 2018.

[37] Dongjiang Li, Dmitry Danilov, Zhongru Zhang, Huixin Chen, Yong Yang, and Peter HL Notten. Modeling the sei-formation on graphite electrodes in lifepo4 batteries. *Journal of The Electrochemical Society*, 162(6):A858, 2015.

[38] Jie Li, Yun Cheng, Ming Jia, Yiwei Tang, Yue Lin, Zhian Zhang, and Yexiang Liu. An electrochemical–thermal model based on dynamic responses for lithium iron phosphate battery. *Journal of Power Sources*, 255:130–143, 2014.

[39] Jialin Liang, Yunhua Gan, Mengliang Yao, and Yong Li. Numerical analysis of capacity fading for a lifepo4 battery under different current rates and ambient temperatures. *International Journal of Heat and Mass Transfer*, 165:120615, 2021.

[40] Rahul Malik, Aziz Abdellahi, and Gerbrand Ceder. A critical review of the li insertion mechanisms in lifepo4 electrodes. *Journal of the electrochemical society*, 160(5):A3179, 2013.

[41] Mohamed Abdel Monem, Khiem Trad, Noshin Omar, Omar Hegazy, Bart Mantels, Grietus Mulder, Peter Van den Bossche, and Joeri Van Mierlo. Lithium-ion batteries: Evaluation study of different charging methodologies based on aging process. *Applied Energy*, 152:143–155, 2015.

[42] Ganesan Nagasubramanian. Two-and three-electrode impedance studies on 18650 li-ion cells. *Journal of power sources*, 87(1-2):226–229, 2000.

[43] Maik Naumann, Michael Schimpe, Peter Keil, Holger C Hesse, and Andreas Jossen. Analysis and modeling of calendar aging of a commercial lifepo4/graphite cell. *Journal of Energy Storage*, 17:153–169, 2018.

[44] Naoki Nitta, Feixiang Wu, Jung Tae Lee, and Gleb Yushin. Li-ion battery materials: present and future. *Materials today*, 18(5):252–264, 2015.

[45] SA Novikova and AB Yaroslavtsev. Lithium deintercalation/intercalation processes in cathode materials based on lithium iron phosphate with the olivine structure. *Russian Chemical Bulletin*, 66(8):1336–1344, 2017.

[46] Akshaya K Padhi, Kirakodu S Nanjundaswamy, and John B Goodenough. Phospho-olivines as positive-electrode materials for rechargeable lithium batteries. *Journal of the electrochemical society*, 144(4):1188, 1997.

[47] Riccardo Poli, James Kennedy, and Tim Blackwell. Particle swarm optimization. *Swarm intelligence*, 1(1):33–57, 2007.

[48] Eric Prada, D Di Domenico, Yann Creff, J Bernard, Valérie Sauvant-Moynot, and François Huet. Simplified electrochemical and thermal model of lifepo4-graphite li-ion batteries for fast charge applications. *Journal of The Electrochemical Society*, 159(9):A1508, 2012.

[49] Shalini Rodrigues, NSAK Munichandraiah, and AK Shukla. Ac impedance and state-of-charge analysis of a sealed lithium-ion rechargeable battery. *Journal of Solid State Electrochemistry*, 3(7):397–405, 1999.

[50] Michael A Roscher, Jens Vetter, and Dirk Uwe Sauer. Characterisation of charge and discharge behaviour of lithium ion batteries with olivine based cathode active material. *Journal of Power sources*, 191(2):582–590, 2009.

[51] Michael A Roscher, Jens Vetter, and Dirk Uwe Sauer. Cathode material influence on the power capability and utilizable capacity of next generation lithium-ion batteries. *Journal of Power Sources*, 195(12):3922–3927, 2010.

[52] E Sarasketa-Zabala, Frederic Aguesse, Igor Villarreal, LM Rodriguez-Martinez, Carmen M López, and Pierre Kubiak. Understanding lithium inventory loss and sudden performance fade in cylindrical cells during cycling with deep-discharge steps. *The Journal of Physical Chemistry C*, 119(2):896–906, 2015.

[53] E Sarasketa-Zabala, I Gandiaga, E Martinez-Laserna, LM Rodriguez-Martinez, and I Villarreal. Cycle ageing analysis of a lifepo4/graphite cell with dynamic model validations: Towards realistic lifetime predictions. *Journal of Power Sources*, 275:573–587, 2015.

[54] E Sarasketa-Zabala, I Gandiaga, LM Rodriguez-Martinez, and I Villarreal. Calendar ageing analysis of a lifepo4/graphite cell with dynamic model validations: Towards realistic lifetime predictions. *Journal of Power Sources*, 272:45–57, 2014.

[55] M. Sedzik. Study of temperature-related aging of lithium-ion battery through an innovative methodology for the determination of physical-model parameters. Master's thesis, Energy Engineering, 2019-20.

[56] Mohammad Shahjalal, Probir Kumar Roy, Tamanna Shams, Ashley Fly, Jahedul Islam Chowdhury, Md Rishad Ahmed, and Kailong Liu. A review on second-life of li-ion batteries: prospects, challenges, and issues. *Energy*, 241:122881, 2022.

[57] Franz B Spingler, Maik Naumann, and Andreas Jossen. Capacity recovery effect in commercial lifepo4/graphite cells. *Journal of The Electrochemical Society*, 167(4):040526, 2020.

[58] Venkat Srinivasan and John Newman. Discharge model for the lithium iron-phosphate electrode. *Journal of the Electrochemical Society*, 151(10):A1517, 2004.

[59] Venkat Srinivasan and John Newman. Existence of path-dependence in the lifepo4 electrode. *Electrochemical and solid-state letters*, 9(3):A110, 2006.

[60] Daniel-Ioan Stroe, Maciej Swierczynski, Ana-Irina Stroe, Søren Knudsen Kaer, and Remus Teodorescu. Lithium-ion battery power degradation modelling by electrochemical impedance spectroscopy. *IET Renewable Power Generation*, 11(9):1136–1141, 2017.

[61] Lars Ole Valøen and Jan N Reimers. Transport properties of lipf6-based li-ion battery electrolytes. *Journal of The Electrochemical Society*, 152(5):A882, 2005.

[62] Pallavi Verma, Pascal Maire, and Petr Novák. A review of the features and analyses of the solid electrolyte interphase in li-ion batteries. *Electrochimica Acta*, 55(22):6332–6341, 2010.

[63] Fenfen Wang, Yelin Deng, and Chris Yuan. Design and cost modeling of high capacity lithium ion batteries for electric vehicles through a techno-economic analysis approach. *Procedia Manufacturing*, 49:24–31, 2020.

[64] Lithium Werks. Datasheet anr26650-m1b 2022.

[65] Borong Wu, Yonghuan Ren, and Ning Li. Lifepo4 cathode material. *Electric Vehicles-The Benefits and Barriers*, pages 199–216, 2011.

[66] Jing Xie and Yi-Chun Lu. A retrospective on lithium-ion batteries. *Nature communications*, 11(1):1–4, 2020.

[67] Kang Xu. Electrolytes and interphases in li-ion batteries and beyond. *Chemical reviews*, 114(23):11503–11618, 2014.

[68] Yonghuang Ye, Yixiang Shi, and Andrew AO Tay. Electro-thermal cycle life model for lithium iron phosphate battery. *Journal of Power Sources*, 217:509–518, 2012.

[69] Masaki Yoshio, Ralph J Brodd, and Akiya Kozawa. *Lithium-ion batteries*, volume 1. Springer, 2009.

[70] Zhi-Hui Zhan, Jun Zhang, Yun Li, and Henry Shu-Hung Chung. Adaptive particle swarm optimization. *IEEE Transactions on Systems, Man, and Cybernetics, Part B (Cybernetics)*, 39(6):1362–1381, 2009.

[71] Hao Zhang, Yang Yang, Dongsheng Ren, Li Wang, and Xiangming He. Graphite as anode materials: Fundamental mechanism, recent progress and advances. *Energy Storage Materials*, 36:147–170, 2021.

[72] Liqiang Zhang, Chao Lyu, Gareth Hinds, Lixin Wang, Weilin Luo, Jun Zheng, and Kehua Ma. Parameter sensitivity analysis of cylindrical lifepo4 battery performance using multi-physics modeling. *Journal of The Electrochemical Society*, 161(5):A762, 2014.

[73] Yancheng Zhang, Chao-Yang Wang, and Xidong Tang. Cycling degradation of an automotive lifepo4 lithium-ion battery. *Journal of power sources*, 196(3):1513–1520, 2011.

[74] Juner Zhu, Ian Mathews, Dongsheng Ren, Wei Li, Daniel Cogswell, Bobin Xing, Tobias Sedlatschek, Sai Nithin R Kantareddy, Mengchao Yi, Tao Gao, et al. End-of-life or second-life options for retired electric vehicle batteries. *Cell Reports Physical Science*, 2(8):100537, 2021.

Abstract in lingua italiana

A fronte della costante crescita di interesse da parte di pubblico e ora anche di imprese commerciali a sostegno dell'adozione diffusa di veicoli a basse emissioni, non sorprende che le batterie agli ioni di litio, che attualmente assumono la maggior parte del costo dei veicoli elettrificati ($\approx$ 40% [56, 63]), siano diventate prolifiche nella letteratura di ricerca scientifica e non solo [40]. Quest'ultima è infatti diventata una delle fonti di energia più comunemente utilizzate nei veicoli di nuova generazione grazie alle sue caratteristiche di alta densità di energia, alta densità di potenza, basso tasso di autoscarica, ecc. [19]. Tuttavia, la vita utile ancora limitata, frena l'ulteriore diffusione dei veicoli elettrici. Per questo motivo i meccanismi di invecchiamento e l'impatto della degradazione della batteria dovrebbero essere considerati come fattori importanti nell'ottimizzazione della progettazione e della gestione del funzionamento di quest'ultima [24]. Tuttavia, l'individuazione e la comprensione dei suddetti fenomeni di invecchiamento è un compito impegnativo a causa dell'interdipendenza tra i vari meccanismi di degradazione che si manifestano sotto forma di perdita di capacità e di potenza [30].
Pertanto, lo scopo di questo lavoro è quello di acquisire conoscenze approfondite sulle modalità di degradazione a lungo termine, analizzando misure sperimentali effettuate su campioni invecchiati in reali applicazioni automotive. A queste viene poi accoppiato un algoritmo di ottimizzazione che, a partire da un insieme di misure sperimentali facilmente acquisibili, permette di calibrare i parametri rappresentatitivi dei fenomeni di degrado. Ciò permetterà di formulare un protocollo di misure in grado di dare una stima dello stato di salute dei campioni di batterie. Infine, è stato eseguito un breve approfondimento sulla diagnostica dei paralleli di celle. Quest'ultimo costituisce il primo passo verso lo studio dei metodi di diagnostica su moduli di celle ancora assemblati.

Parole chiave: batterie agli ioni di litio, degradazione di tipo automotive, veicoli elettrici, diagnostica sperimentale, modello fisico